

Stopping Self-Discharge in Metal-Air Batteries

by

Brandon J. Hopkins

S.M. Mechanical Engineering
Massachusetts Institute of Technology, 2013

A.B. Engineering Sciences
Harvard University, 2011

SUBMITTED TO THE DEPARTMENT OF MECHANICAL ENGINEERING IN PARTIAL
FULFILLMENT OF THE REQUIREMENTS FOR THE DEGREE OF

DOCTOR OF PHILOSOPHY IN MECHANICAL ENGINEERING
AT THE
MASSACHUSETTS INSTITUTE OF TECHNOLOGY

JUNE 2018

© 2018 Massachusetts Institute of Technology
All rights reserved.

Signature of Author: _____ **Signature redacted**

Department of Mechanical Engineering
May 17, 2018

Certified by: _____ **Signature redacted**

Douglas P. Hart
Professor of Mechanical Engineering
Thesis Supervisor

Accepted by: _____ **Signature redacted**

Rohan Abeyaratne
Quentin Berg Professor of Mechanics
Chairman, Committee on Graduate Students



Stopping Self-Discharge in Metal-Air Batteries

by

Brandon J. Hopkins

Submitted to the Department of Mechanical Engineering
on May 17, 2018 in partial fulfillment of the requirements for the degree of
Doctor of Philosophy in Mechanical Engineering

Abstract

Metal-air batteries boast high theoretical energy densities, but negative electrode corrosion can severely reduce their usable capacity and commercial utility. Most methods to mitigate corrosion focus on electrode and electrolyte modification such as electrode alloying, electrolyte additives, and gel and nonaqueous electrolytes. These methods, however, either insufficiently suppress the parasitic reaction or compromise power and energy density. This thesis focuses on a different approach to corrosion mitigation involving electrolyte displacement from the electrode surface. Multiple electrolyte-displacement concepts were generated and investigated. The most promising of the concepts was the reversible displacement of the electrolyte from the electrode surface with an oil. To enable this method, the fundamental physics of underwater oil-fouling resistant surfaces was investigated, tested, and characterized. Design equations that aid in the appropriate selection of electrodes, displacing oils, and separator membranes were also developed. The oil displacement method was demonstrated in a primary (single-use) aluminum-air (Al-air) battery that achieved a 420% increase in useable energy density and was estimated to enable pack-level energy densities as high as 700 Wh l^{-1} and 900 Wh kg^{-1} . This method could, in principle, be used in any of the metal-air batteries, aqueous or nonaqueous, or in other energy storage systems that suffer from corrosion if appropriate displacing oils and separator membranes are found using the discussed design principles. With the oil displacement method, aqueous metal-air batteries that rely on abundant, broadly dispersed materials could provide safe, low-cost, sustainable primary and secondary (rechargeable) batteries for many applications including grid-storage, off-grid storage, robot power, and vehicular propulsion.

Thesis Supervisor: Douglas P. Hart
Title: Professor of Mechanical Engineering

Acknowledgments

I thank professor Douglas P. Hart for being a wonderful thesis advisor. I am grateful for professors Yang Shao-Horn, Alexander H. Slocum, and Thomas W. Eagar for supporting me as members of my thesis committee. I thank the members of Professor Hart and Professor Shao-Horn's lab for their many helpful conversations and encouragement. I am grateful for my supportive wife, parents, and siblings and acknowledge God's hand in my life.

Table of Contents

Abstract.....	3
Acknowledgments.....	4
Table of Contents.....	5
List of Figures.....	8
Chapter 1: Introduction.....	10
1.1 Research Objectives.....	10
1.2 Metal-Air Batteries.....	11
1.3 Negative Electrode Corrosion.....	14
Chapter 2: Existing Corrosion Mitigation Methods.....	16
2.1 Chapter Summary.....	16
2.2 Negative Electrode Alloying and Electrolyte Additives.....	16
2.3 Alternative Electrolytes.....	18
2.4 Electrolyte Draining and Electrode Washing.....	19
2.5 Other Corrosion Mitigation Methods.....	19

Chapter 3: Corrosion Mitigation Concept Generation and Selection	21
3.1 Chapter Summary.....	21
3.2 Design Requirements.....	21
3.3 Passive Sacrificial Anode.....	22
3.4 Impressed Current Cathodic Protection.....	22
3.5 Electrolyte Filtration.....	23
3.6 Temperature and Pressure Control.....	24
3.7 Temporary Anodization.....	25
3.8 Negative Electrode Wiper.....	25
3.9 Displacing Sponge.....	26
3.10 Louver Gasket.....	27
3.11 Ferrofluid Displacement.....	27
3.12 Fluid Displacement.....	28
3.13 Concept Comparison and Selection.....	33
Chapter 4: Oil Displacement of Electrolyte	34
4.1 Chapter Summary.....	34
4.2 Oil Displacement of Electrolyte.....	34
4.3 Al-Air Test Cell Design and Operation.....	36
4.4 Pumping and Air-Feed Power Requirements.....	38
4.5 Oil and Separator Membrane Selection.....	41
4.6 Endurance Testing.....	48

4.7 Cell Characterization.....50

4.8 Pack-Level Energy Density.....55

4.9 Pumping Optimization.....59

Chapter 5: Conclusion.....63

5.1 Purpose, Importance, Impact.....63

5.2 Accomplishments.....64

5.3 Future Work.....65

Works Cited.....67

List of Figures

Fig. 1.1 Comparison of practical energy densities of Li-ion and metal-air batteries.....	12
Fig. 1.2 Abundance of elements in the Earth's crust.....	13
Fig. 1.3 Schematic of metal-air battery.....	14
Fig. 2.1 Performance tradeoff between corrosion-mitigation methods.....	18
Fig. 3.1 Schematic of NaOH electrolyte filtration concept.....	23
Fig. 3.2 Schematic of negative electrode wiper.....	25
Fig. 3.3 Exploded view of displacing sponge prototype CAD model.....	26
Fig. 3.4 Louver gasket concept.....	27
Fig. 3.5 Ferrofluid concept testing.....	28
Fig. 3.6 Schematic of air-displacement concept.....	29
Fig. 3.7 Exploded view of Al-air prototype.....	30
Fig. 3.8 Schematic of oil-displacement concept.....	31
Fig. 3.9 On-off cycling test comparing post-drain wash and oil displacement methods.....	32
Fig. 3.10 Design concept comparison.....	33
Fig. 4.1 Oil displacement method.....	35
Fig. 4.2 Exploded view of Al-air test cell.....	37

Fig. 4.3 Contact angle images with advancing and receding contact angle values.....	44
Fig. 4.4 Selecting a displacing oil and separator membrane.....	48
Fig. 4.5 Voltage vs. gravimetric energy density at a discharge rate of $150 \text{ mA cm}_{\text{geo}}^{-2}$ with and without hydrophilic PTFE separator membrane.....	48
Fig. 4.6 24-day on-off cycling.....	49
Fig. 4.7 Constructed-cell performance.....	51
Fig. 4.8 Current density vs. time with and without hydrophilic PTFE separator membrane.....	53
Fig. 4.9 Voltage vs. time with hydrophilic PTFE separator membrane.....	53
Fig. 4.10 Voltage and power density vs. current density with and without hydrophilic PTFE separator membrane.....	54
Fig. 4.11 Gravimetric energy density vs. current density with the hydrophilic PTFE separator membrane.....	54
Fig. 4.12 Pack-level mass distribution.....	55
Fig. 4.13 Useable system energy density.....	57
Fig. 4.14 Losses due to corrosion after pumping.....	60
Fig. 4.15 Pumping and corrosion losses after shutdown.....	62

Chapter 1

Introduction

1.1 Research Objectives

The goal of this thesis is to stop self-discharge in metal-air batteries induced by negative electrode corrosion. Metal-air batteries have impressive theoretical energy densities [1]–[3], but negative electrode corrosion can induce severe self-discharge rates of more than 100% a month while Li-ion batteries self-discharge only 5% a month [4]. Existing methods to mitigate corrosion typically involve chemically modifying the battery's negative electrode and electrolyte. This thesis, however, focuses on a much less investigated area of corrosion mitigation involving the mechanical displacement of the corrosive electrolyte from the negative electrode surface. This approach was taken because chemical mitigation methods commonly require a significant performance tradeoff between power and energy density and open-circuit corrosion. In contrast, mechanical methods have the potential to largely sidestep this performance tradeoff. If the tradeoff between power and energy density and open-circuit corrosion could be sufficiently mitigated, the use of metal-air batteries could be extended far beyond current niche applications

[3]. Given this opportunity, ***the objective of this thesis was to create and test energy-dense electrolyte displacement strategies to mitigate open-circuit corrosion in metal-air batteries.***

Primary (single-use) aluminum-air batteries served as the model system for testing in this study.

1.2 Metal-Air Batteries

Metal-air batteries are one of the promising electrochemical energy storage candidates [5]. They are generally more energy dense (Fig. 1.1) and potentially lower cost than Li-ion batteries [1]–[3], [6], [7]. Lithium-ion is currently the dominant energy storage technology for many applications despite concerns regarding its cost [8], safety [9]–[11], availability [12], [13], and recyclability [14]. Elements such as iron, zinc, magnesium, and aluminum are desirable candidates for use in next generation batteries because of their abundance (Fig.1.2), recyclability, lightweight, safety, low cost, and two to three-electron redox properties. Such metals can be used as negative electrodes in aqueous metal-air batteries that use oxygen from the air as a primary reactant and allow for decreased battery weights and volumes [1], [3].

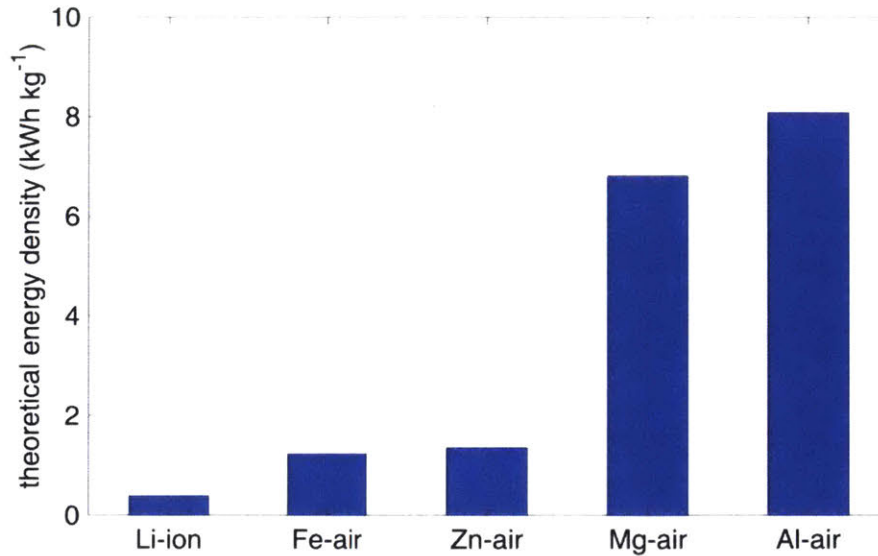
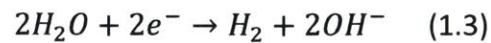
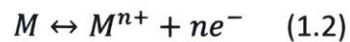
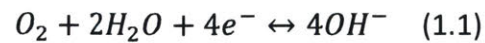


Fig. 1.1 Comparison of practical energy densities of Li-ion and metal-air batteries [3].

Metal-air batteries generally consist of a metal electrode, electrolyte, separator membrane, and air electrode (Fig. 1.3). The positive electrode is an air electrode consisting of carbon particles pressed on a metal mesh with a catalyst resulting in the reaction shown in Eq. 1.1. The negative electrode is a metal (M), which undergoes the reaction shown in Eq. 1.2. The parasitic corrosion reaction (Eq. 1.3), which this thesis aims to suppress when the battery is not in use, results in hydrogen evolution and is shared among aqueous metal-air batteries.



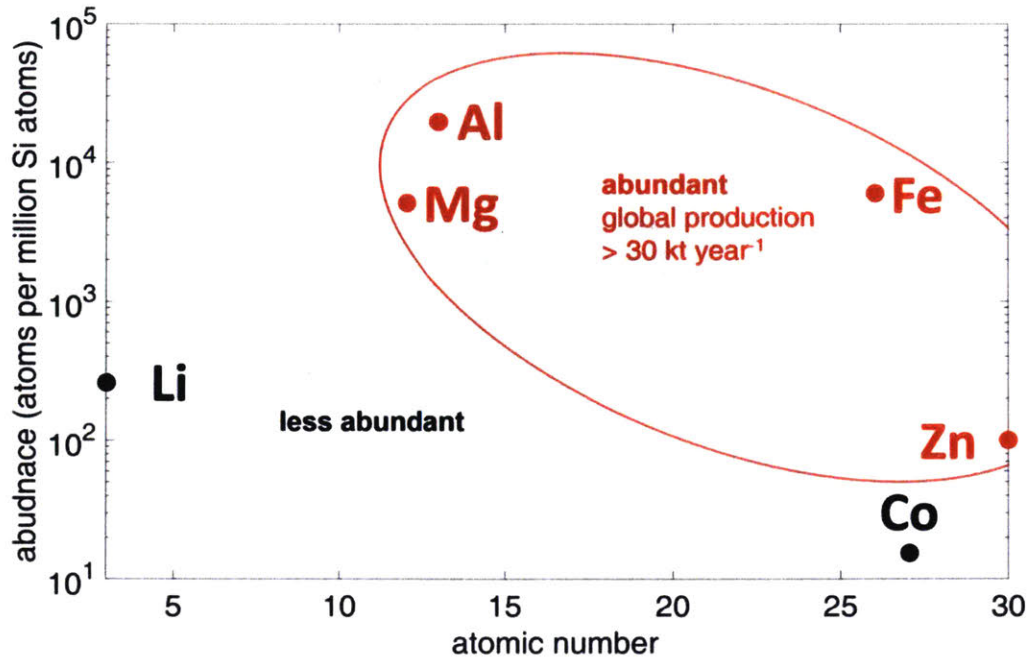


Fig. 1.2 Abundance of elements in Earth's crust [15]. Al, Fe, Mg, and Zn are highly abundant elements while Li and Co, both used in Li-ion batteries, are generally less abundant.

Some aqueous metal-air chemistries allow for secondary (rechargeable) batteries such as zinc-air and iron-air while aluminum-air and magnesium-air are typically primary (single-use) batteries. Most metal-air batteries can be mechanically rechargeable by designing the cell pack so that the metal electrodes can be easily replaced once they are fully consumed [16]. There are also nonaqueous metal-air batteries. For example, Li-air batteries are commonly nonaqueous because they typically use nonaqueous electrolytes due to lithium's reactivity with water. While Li-air batteries have the largest theoretical energy density, they still face a variety of challenges [17]. To date, zinc-air batteries used in hearing aids have arguably been the most commercially successful metal-air battery [3].

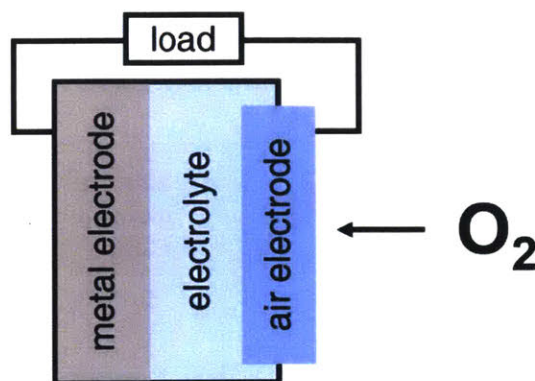


Fig. 1.3 Schematic of a metal-air battery.

1.3 Negative Electrode Corrosion

A long-standing barrier to increased commercialization for aqueous metal-air batteries has been severe open-circuit corrosion that induces unacceptably high self-discharge rates for many applications. Corrosion mitigation strategies for metal-air batteries have been a topic of significant discussion for many decades [18]. Despite impressive recent advances in corrosion inhibition, metal-air batteries still suffer from severe open-circuit corrosion. For example, some of the lowest corrosion currents reported in the literature for Zn, Mg, and Al are 0.05, 1.3, and 2 mA cm_{geo}⁻² respectively [19]–[21] in aqueous electrolytes. Assuming a 10 cm by 10 cm by 0.5 cm planar electrode that is continuously surrounded by electrolyte, a Zn, Mg, and Al electrode will self-discharge at rates of 3%, 109%, and 80% per month based on mass using Faraday’s law of electrolysis [22]. As an explicit example, after one month of continuous contact with electrolyte, 80% of the mass of an Al electrode will have dissolved into the electrolyte assuming the electrolyte is not saturated. The 0.05 mA cm_{geo}⁻² corrosion current for zinc, however, is for a mirror-polished surface [19]. In practice, zinc electrodes are commonly fabricated in sponge,

fiber, or powder-bed forms with large surface-to-volume ratios to enhance activity [23]. Assuming a zinc electrode made up of zinc spheres with diameters of 100- μm [24], the self-discharge rate will be 187% per month, which is unacceptable for many applications. For example, imagine a zinc-air powered vehicle that was recently charged up and then not used for one week. By the end of the week, almost half of the charge in the battery would be depleted.

Chapter 2

Existing Corrosion Mitigation Methods

2.1 Chapter Summary

Existing methods to inhibit corrosion are presented. Methods include negative electrode alloying, electrolyte additives, nonaqueous electrolytes, gel electrolytes, and draining the electrolyte after shutdown. Electrode alloying and electrolyte additives allow for high power and energy density but poor corrosion inhibition. Nonaqueous and gel electrolytes, conversely, achieve poor power and energy density but minimal corrosion. Electrolyte draining can result in significant corrosion and hazardous clogging of the hydraulic system of metal-air battery packs. A post-drain wash can improve restart performance, but reduces system energy density.

2.2 Negative Electrode Alloying and Electrolyte Additives

Existing corrosion mitigation methods typically require a tradeoff between corrosion performance and power and energy density (Fig. 2.1). Alloying combined with electrolyte

additives in an aqueous electrolyte yields high power and energy density but high corrosion [25]. For the purposes of this study, specific corrosion mitigation methods found in the Al-air literature are provided, but similar methods are used for other metal-air batteries. Binary, ternary, and quaternary aluminum alloys have been created to mitigate open-circuit corrosion. Alloying elements have included Hg [26], Zn [26]–[30], In [27], [28], [31]–[34], Mg [26], [29], [32]–[35], Ga [31], [32], [34]–[38], Sn [27]–[30], [36], [38]–[40], Bi [27], B [40], Ti [32], Pb [41], [42], and Mn [29], [32]–[34]. Alloying high purity and commercial aluminums have also been investigated [27], [43]–[47]. Additionally, Ferrando and Mori created corrosion-inhibiting anode composites using polymers [48] and ceramics [49], [50] respectively. Electrolyte additives such as ZnO [26], [43], [51], SnO_3^{2-} , $\text{In}(\text{OH})_3$, BiO_3^{3-} , $\text{Ga}(\text{OH})_4^-$, MnO_4^{2-} [52], Cl^- , NO_3^- , SO_4^{2-} [53], stannate [54], [55], cationic surfactants [26], [56], [57], lupine seed extract [57], polyacrylic acid [58], and organic inhibitors [59], [60] have also been tested.

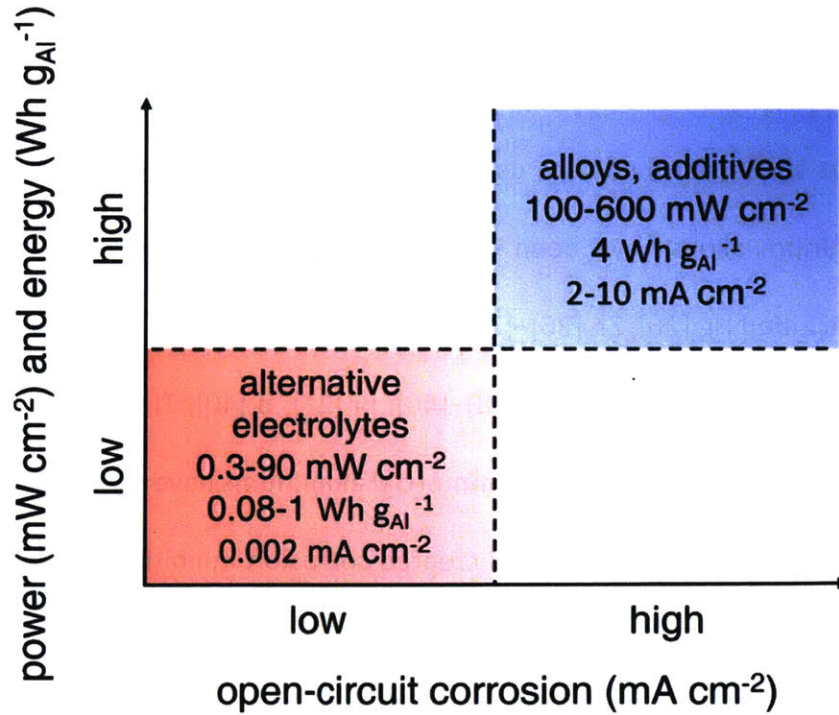


Fig. 2.1 Performance tradeoff between corrosion-mitigation methods [18], [21], [25], [61]–[63].

2.3 Alternative Electrolytes

Nonaqueous and gel electrolytes generally achieve lower corrosion rates but only fractions of the power (Fig. 2.1) and energy density achieved by the more conductive aqueous electrolytes [62]–[64]. Alternative electrolytes including alcohols [65]–[68], sulfuric acid [69], non-aqueous electrolytes [70], solid polymer electrolyte membranes [71], gels [62], [72], ionic liquid-water solutions [73], and hybrid inorganic/organic systems [21] have been explored.

2.4 Electrolyte Draining and Electrode Washing

Draining the electrolyte after shutdown can result in significant electrode corrosion and hazardous clogging of the hydraulic system of metal-air battery packs [74], [75]. After draining, thin films of remaining electrolyte cling to the hydrophilic metal electrodes, induce corrosion, dry up, and leave crusts of by-products and electrolyte solutes. Rinsing the negative electrode with water or a pH-neutralizing agent after electrolyte draining improves restart performance but can significantly reduce system energy densities if the rinsing system is contained in the battery pack [75], [76]. Such rinsing systems require additional tanks for water and electrolyte along with a neutralizing agent that is consumed with every shutdown [75], [76].

2.5 Other Corrosion Mitigation Methods

Other less commonly used, but also interesting and promising corrosion mitigation methods, include the following strategies. Some have investigated anode grain structure modification [77]–[79]. Others have dealt with corrosion by connecting Al-air batteries to hydrogen fuel cells to use the emitted hydrogen gas [80]. Dual-electrolyte systems that use a less corrosive electrolyte near the aluminum anode and an aqueous electrolyte near the cathode have also been tested [81]. One group proposed the use of a gel electrolyte that can separate from the negative electrode to mitigate open-circuit corrosion [62]. The performance of many common and specialized corrosion mitigation methods have been compared by Egan, Ponce de León, Jones, Stokes, and Walsh [18]. In summary, the corrosion mitigation methods presented in this chapter either

insufficiently suppress the parasitic reaction or significantly compromise power and energy density (Fig. 2.1).

Chapter 3

Corrosion Mitigation Concept Generation and Selection

3.1 Chapter Summary

Several design concepts focused on mitigating negative electrode corrosion are presented. Initial judgment on generated concepts was suspended to allow for room to explore unusual ideas. From this process, the oil displacement method emerged as a promising corrosion mitigation concept.

3.2 Design Requirements

The corrosion mitigation concept should meet the following criteria.

1. Be compatible with a variety of negative electrode architectures, i.e. pellet, fiber, or planar electrodes.
2. Enable an open-circuit self-discharge rate of 5% or less.

3. Require minimal energy for startup/shutdown cycles.
4. Add minimal mass and volume to the battery pack.
5. Require no energy during battery storage.
6. Be cost appropriate.

3.3 Passive Sacrificial Anode

Passive sacrificial anodes are used on ship hulls to reduce corrosion. For example, if a ship was made of steel, zinc would be an appropriate sacrificial anode material because zinc has a more negative electrode potential than steel in seawater [22]. Applying such a strategy to suppress corrosion in a battery would likely not be successful because even materials that have very large negative electrode potentials such as aluminum, zinc, and magnesium corrode too quickly as discussed in section 1.4 Negative Electrode Corrosion. To rigorously develop the concept, the corrosion potential for each metal in a specific electrolyte would have to be measured and then ranked to identify a potential sacrificial anode material.

3.4 Impressed Current Cathodic Protection

Impressed current cathodic protection is used on large structures to stop corrosion [22]. Such a system would be impractical for a battery pack. The anode experiences minimal corrosion because the power supply effectively provides the electrons. If such a system was used for a steel structure submerged in water, dissolved chloride ions from the surrounding ocean turn into chlorine gas. At the protected steel surface, hydroxides are formed. For a battery system, it is

unclear what acceptable reaction could occur at the impressed-current anode. Additionally, the formations of hydroxides at the protected electrode surface would be very undesirable as their constant formation would continually increase the pH of the electrolyte.

3.5 Electrolyte Filtration

Much like a water filter can remove salts, the high or low-pH electrolyte solutions of metal-air batteries could be temporarily filtered when the battery is not in use so that a neutral pH solution is in direct contact with the negative electrode (Fig. 3.1). The concentration of salt in seawater (0.6 M NaCl) is minimal in comparison to the concentration of sodium hydroxide in an Al-air battery electrolyte (4 M NaOH).

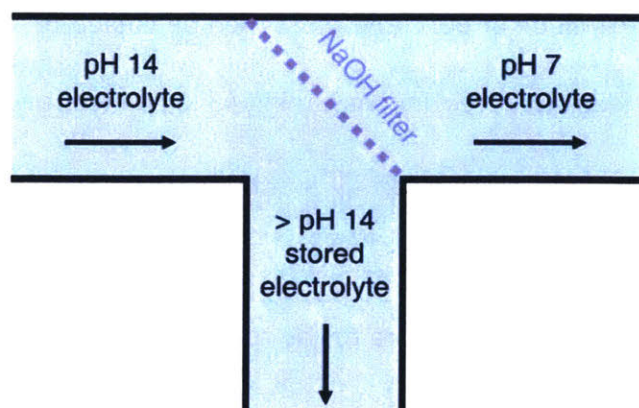


Fig. 3.1 Schematic of NaOH electrolyte filtration concept.

However, for a lower-bound approximation, it is assumed that the amount of energy required to filter out NaOH from the electrolyte is equal to the energy required to filter out salt to potable levels, 1.8 kWh m^{-3} [82]. Assuming 40 l of electrolyte in an Al-air battery pack [25], 72 Wh would

be a lower-bound limit required per startup/shutdown cycle. Most commercially available filters, however, cannot handle such high pH solutions.

3.6 Temperature and Pressure Control

When the battery is not in use, the electrolyte could be frozen to stop corrosion. Using the specific heat formula (Eq. 3.1), the energy required to lower the temperature of the electrolyte can be estimated.

$$Q = mc\Delta T \quad (3.1)$$

The required energy Q [J] is a function of the mass of the material being heated, m [kg], the specific heat of the material, c [$\text{J kg}^{-1} \text{C}^{-1}$], and the change in temperature ΔT [C]. During operation, the electrolyte will be at 60°C and must then be cooled to -20°C when the battery is not in use [83] to start electrolyte freezing. Assuming 45 kg of electrolyte [84], a specific heat of $4000 \text{ J kg}^{-1} \text{C}^{-1}$, and a temperature change of 80°C , 4 kWh of energy would be required.

Another strategy could be to apply pressure to the reaction to stop the generation of hydrogen. However, data in the literature suggests that hydrogen evolution from aluminum can continue above 10 MPa [85], which would likely rupture the air electrodes and pose a safety hazard.

3.7 Temporary Anodization

Anodization is used to protect surfaces from corrosion. Perhaps when the battery is not in use, the electrode could be anodized and then unanodized right before battery use. Anodized surfaces, however, are only protected between a pH of 4 and 8.5 [86] and an Al-air battery's electrolyte generally has a pH of 14.

3.8 Negative Electrode Wiper

A wiper/squeegee could be used to displace the corrosive electrolyte from the surface when the battery is not in use (Fig. 3.2). While this strategy could be effective for planar electrodes, it would only partially displace the electrolyte for pellet or fiber electrodes. It could also be challenging to seal the rest of the electrolyte in the hydraulic system of the battery from the electrode surfaces.

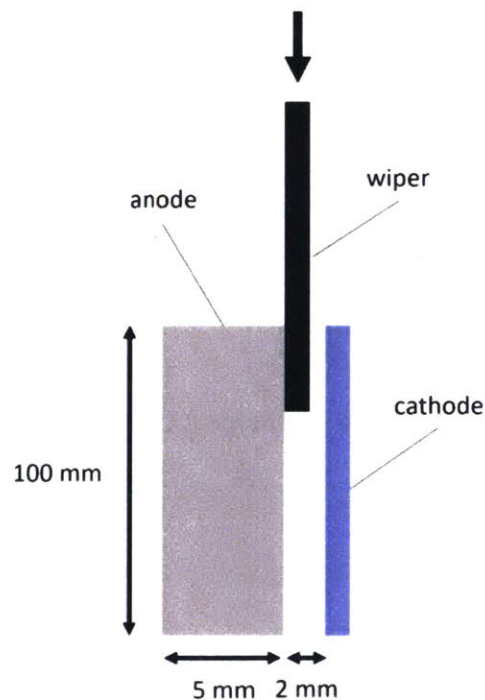


Fig. 3.2 Schematic of negative electrode wiper.

3.9 Displacing Sponge

A foam sponge could be placed in the interelectrode gap of the battery. When the battery is not in use, the electrodes could be pressed together to displace the electrolyte. The sponge would act as a type of fluid displacing seal. A CAD model of a prototype is shown in Fig. 3.3. This model was fabricated by 3D-printing and was tested. While the electrolyte flowed easily through the silicone foam initially, the foam was quickly clogged by reaction byproducts.

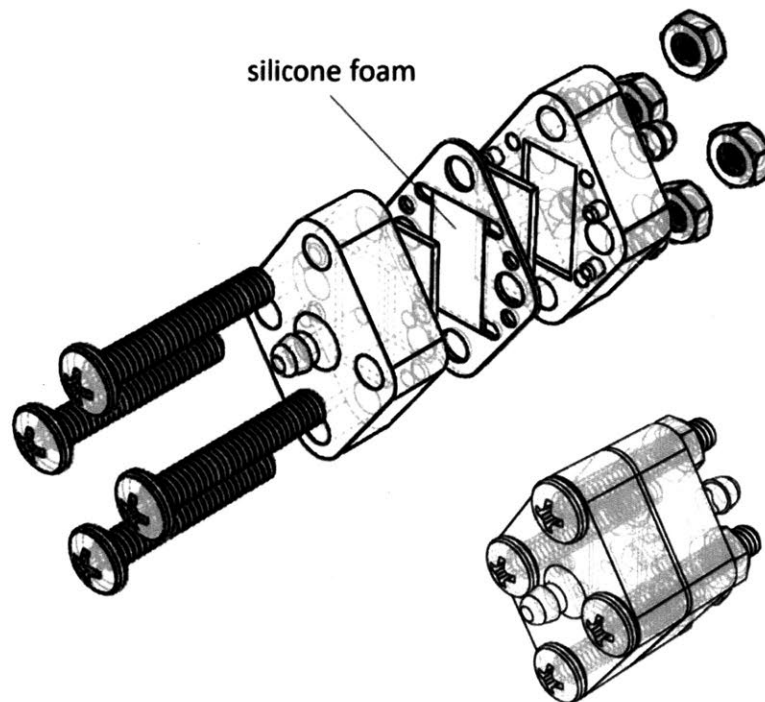


Fig. 3.3 Exploded view of displacing sponge prototype CAD model.

3.10 Louver Gasket

A gasket displaces the corrosive electrolyte from the negative electrode surface when the battery is not in use by moving the positive and negative electrodes toward one another. The gasket is less likely to clog than the displacing sponge. A prototype of a louver gasket was fabricated (Fig. 3.4) by 3D printing with a rubber-like material, Tango Black. The prototype was tested and successfully mitigated corrosion, but would not displace much electrolyte if the negative electrode was made of pellets or fibers. Additionally, the louver gasket would require moving parts that are prone to failure.

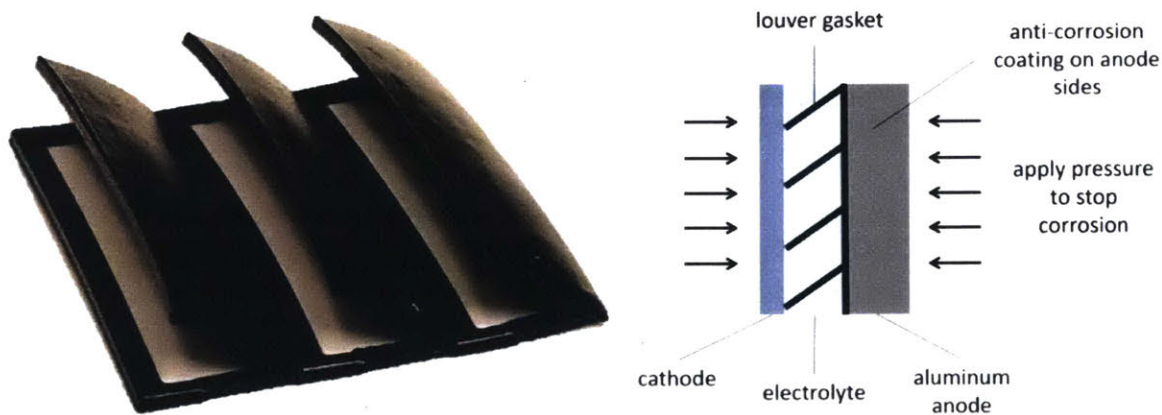


Fig. 3.4 Louver gasket concept. Fabricated gasket (left) and gasket schematic in Al-air cell (right).

3.11 Ferrofluid Displacement

A ferrofluid controlled by magnetic fields could cover the aluminum electrode when the battery is not in use. A bench-top experiment demonstrating this concept was performed. When a piece

of aluminum was covered by the ferrofluid, no more hydrogen evolution was visible when the ferrofluid displaced the corrosive electrolyte from the electrode (Fig. 3.5). The key issue with this tested concept was that the electrolyte reacted with the iron in the ferrofluid, which is why the electrolyte in Fig. 3.5 turned bright yellow. Normally the electrolyte is clear. After a few days of electrolyte exposure, the ferrofluid would eventually clump together and stop functioning appropriately.

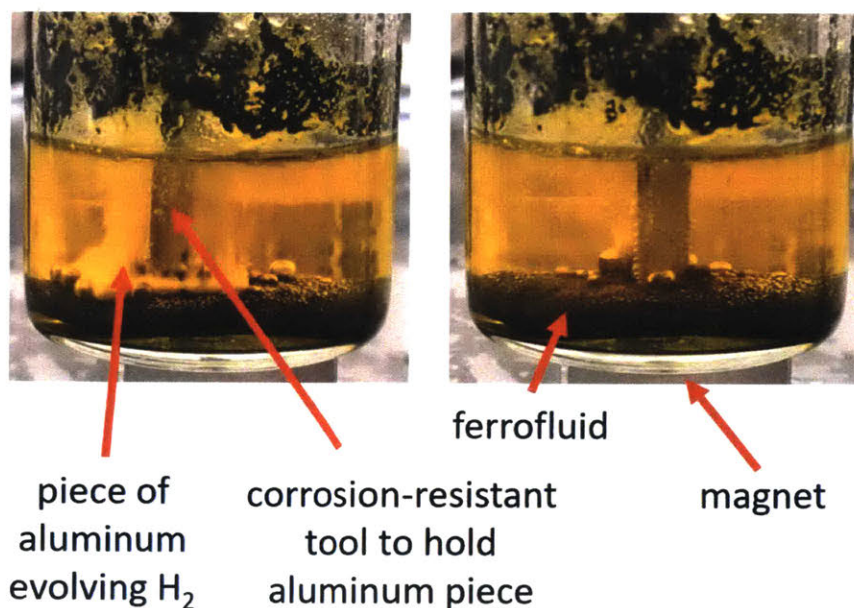


Fig. 3.5 Ferrofluid concept testing. Exposed aluminum piece evolving hydrogen in the yellow-tinted electrolyte (left). Aluminum piece covered by ferrofluid stops evolving hydrogen (right).

3.12 Fluid Displacement

A fluid could be pumped into the Al-air battery when the battery is not in use to displace the corrosive electrolyte from the negative electrode surface. Unlike other strategies, a fluid could be pumped through a pellet or fiber electrode. The thickness of the remaining electrolyte that

clings to the negative electrode surface can be decreased by increasing pumping time or speed. Air that can be approximated as an incompressible fluid at low speeds could be used to displace the electrolyte. Compressed air could push the electrolyte out of the interelectrode gap of the battery. However, air has a low viscosity (10^{-5} Pa s) and would therefore require significant power to scrape off the remaining electrolyte from the sides of the interelectrode gap of the battery (Fig. 3.6).

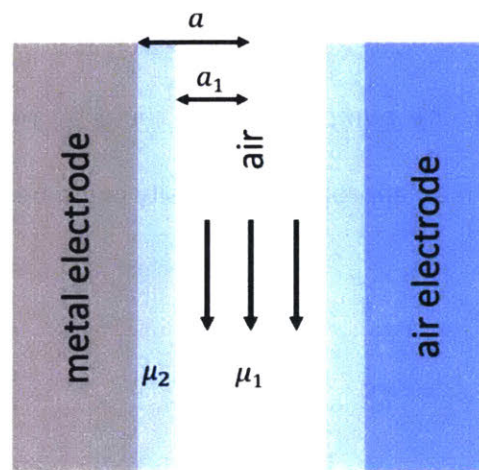


Fig. 3.6 Schematic of air-displacement concept.

To calculate an estimate of the pumping power per unit length along the negative electrode, the following assumptions are made. Flow instabilities are neglected by giving the displacing fluid (viscosity μ_1) the same density as the electrolyte (viscosity μ_2). Laminar flow is assumed, and the air is treated as an incompressible fluid, which is valid for speeds below a Mach number of 0.3. With a channel length of L , a channel height of $2a$ ($2a \ll L$), or more explicitly the variable a multiplied by 2, and channel width of b ($b \sim L$) (coming out of the page), the following relationship is derived (Eq. 3.2). A no-slip boundary condition is applied to both the electrolyte-electrode

interface and the fluid-fluid interface. At the fluid-fluid interface, the shear stresses are assumed to be equal.

$$\mathcal{P}_L = b \left(\frac{\Delta P}{L} \right)^2 \left(\frac{2}{3\mu_2} (a^3 - a_1^3) + \frac{a}{\mu_2} (a^2 - a_1^2) + \frac{2a_1^3}{3\mu_1} \right) \quad (3.2)$$

A constant electrolyte removal rate is fixed by assuming a constant pressure gradient, ΔP . Equation 3.2 shows that the lower the viscosity of the displacing fluid (μ_1) the more pumping power is required. If a more viscous displacing fluid is selected with a viscosity near the viscosity of the electrolyte (10^{-3} Pa s), the pumping power could be reduced by a factor of 100. An alternative displacing fluid with an appropriate viscosity could be an immiscible oil [87].

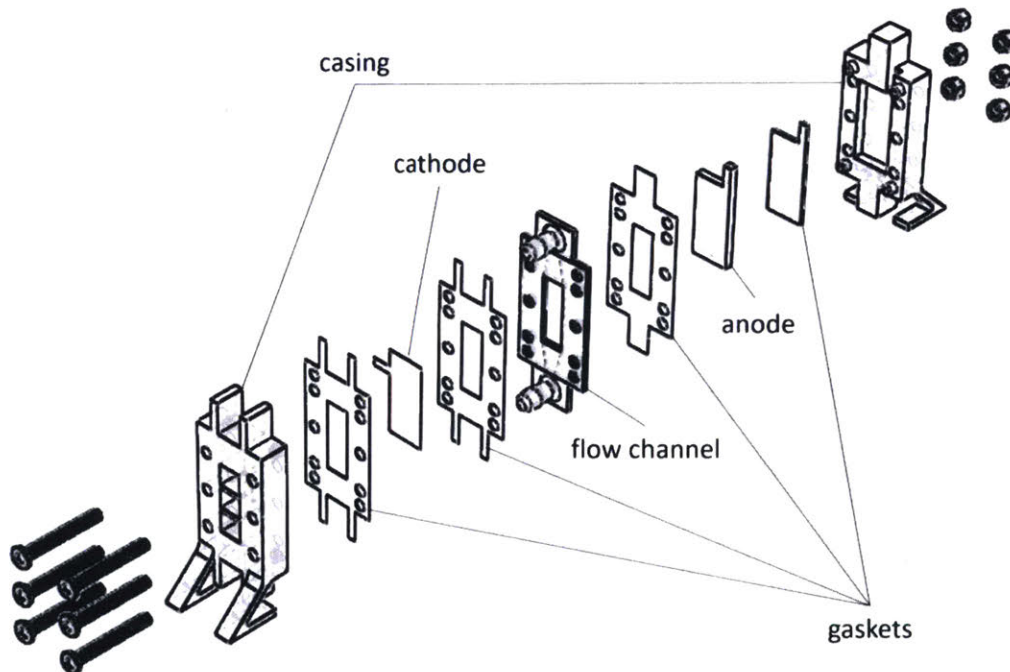


Fig. 3.7 Exploded view of the Al-air prototype.

The viability of this concept was tested using a light viscosity mineral oil and by constructing an Al-air battery with a 3D-printed casing (Fig. 3.7). Gaskets were laser cut out of silicone rubber sheets. The anode was 6.34-mm-thick 99.996% aluminum. The electrolyte was 4 M sodium hydroxide. The cathode was QSI-Nano[®] manganese gas diffusion air electrode (Quantum Sphere). As the schematic shows (Fig. 3.8), oil or electrolyte was pumped into the Al-air test cell via a peristaltic pump.

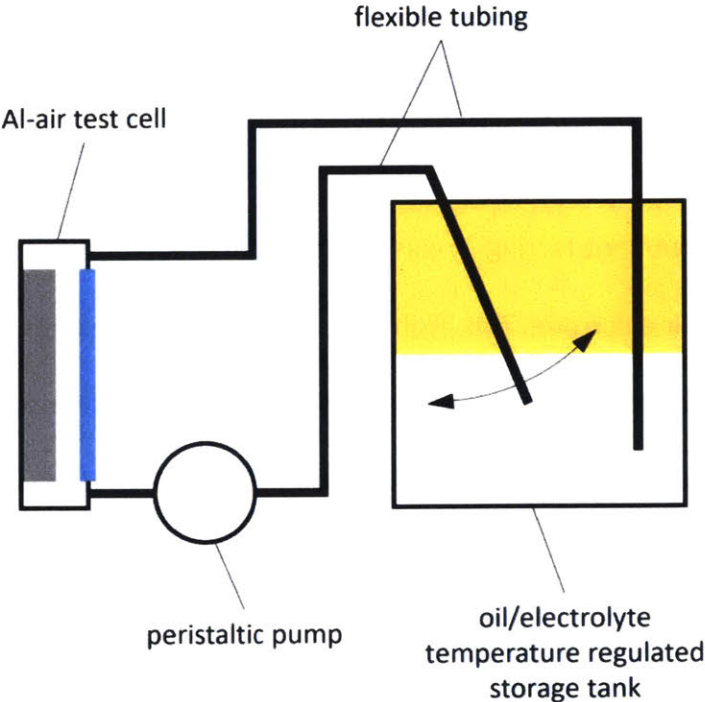


Fig. 3.8 Schematic of the oil-displacement concept.

To compare the oil displacement method to a post-drain wash strategy [75], on-off cycling wherein $0.3 \text{ mA cm}_{\text{geo}}^{-2}$ was drawn for 10 min separated by 10-min pauses was performed. For the post-drain wash portion of the test (highlighted in blue in Fig. 3.9), the electrolyte was drained for 2 min, the electrode was then flushed with pure water for 2 min, and then the water was

drained for 2 min. The gray portions of the graph denote that no current was drawn at that time. There was still a positive voltage even after the post-draining wash had been drained, which was near 1.5 V when no current was being drawn. This positive voltage implies that the electrodes were connected by a water bridge, which means that corrosion may continue after the water had been drained. During the oil displacement portion of the test (highlighted in yellow in Fig. 3.9), negative voltages were observed once the oil was pumped in when no current was being drawn. The negative voltage suggests that the two electrodes were ionically insulated from one another implying that there was little electrolyte left in the interelectrode gap of the battery. The oil flush did not appear to affect the voltage during discharge once the oil was displaced by the electrolyte. After further oil-displacement testing, it was found that if the pauses in discharge were too long, the oil would foul the air electrode. This problem was overcome by adding a separator membrane that allowed for continuous air-electrode hydration and will be discussed in chapter 4. More details about oil-displacement experiments will also be covered in chapter 4.

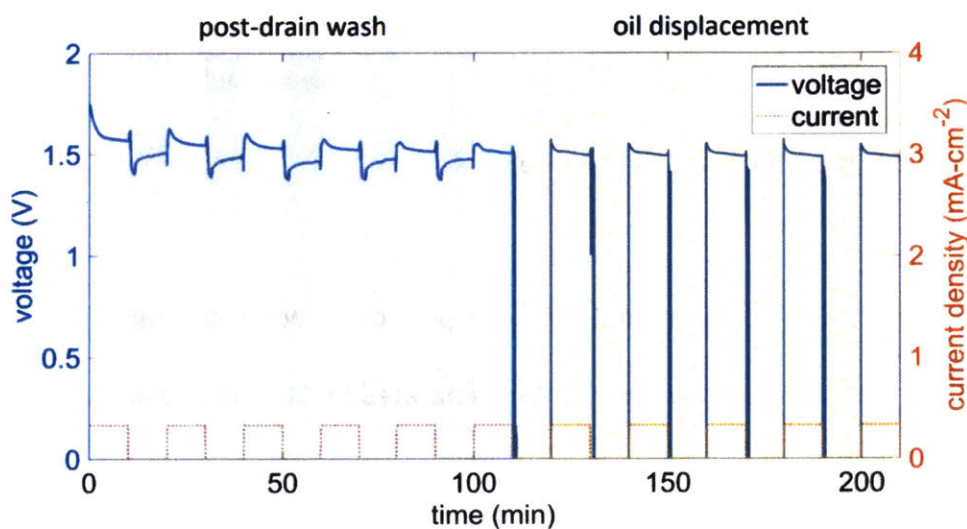


Fig. 3.9 On-off cycling test comparing post-drain wash and oil displacement methods.

3.13 Concept Comparison and Selection

The pros and cons of each of design concept are summarized in Fig. 3.10. Concepts are presented in columns while design requirements and risks are designated by rows. If a box is red, that means the design requirement is not met or that there is a significant risk associated with meeting that design requirement. Boxes in green mean the design requirement is likely met by the design concept. Boxes in yellow denote uncertainty about whether the design requirement is or could be met. Based on the design concept comparison chart, the oil displacement concept was selected for development.

	sacrificial anode	cathodic protection	filtration	T and P control	anodize	wiper	sponge	louver gasket	ferrofluid	oil
electrode compatibility	Y	Y	Y	Y	Y	N	N	N	Y	Y
acceptable discharge rate	N	?	?	?	N	?	?	Y	Y	Y
kWh cycle ⁻¹	?	?	> 0.07	4	?	?	?	Y	?	0.02
risks	corrosion too high	increases electrolyte pH	pH too high for filters	requires continuous energy	electrolyte pH too high	won't displace enough fluid	clogged pores	won't displace enough fluid	reacts with electrolyte	partial electrode fouling

Fig. 3.10 Design concept comparison.

Chapter 4

Oil Displacement of Electrolyte

4.1 Chapter Summary

To test the oil displacement concept, an Al-air cell was constructed that could function as a conventional flowing-electrolyte Al-air battery and an Al-air battery using the oil displacement method. Principles from underwater oleophobicity and thin film rupture theory enabled appropriate oil and separator membrane selection. A 24-day on-off cycling test was performed showing that an Al-air battery using an oil displacement system achieves a 420% increase in useable energy density. An Al-air battery pack using an oil displacement system could achieve pack-level energy densities as high as 700 Wh l^{-1} and 900 Wh kg^{-1} .

4.2 Oil Displacement of Electrolyte

To overcome the problem of long-term open-circuit corrosion, the conventional flowing electrolyte metal-air battery was redesigned (Fig. 4.1A) [61], [75], [88]. An underwater-

oleophobic separator membrane was added to allow for the reversible displacement of corrosive electrolyte from the negative electrode surface with an oil when the battery was not in use (Fig. 4.1B, Fig. 4.1C) [87].

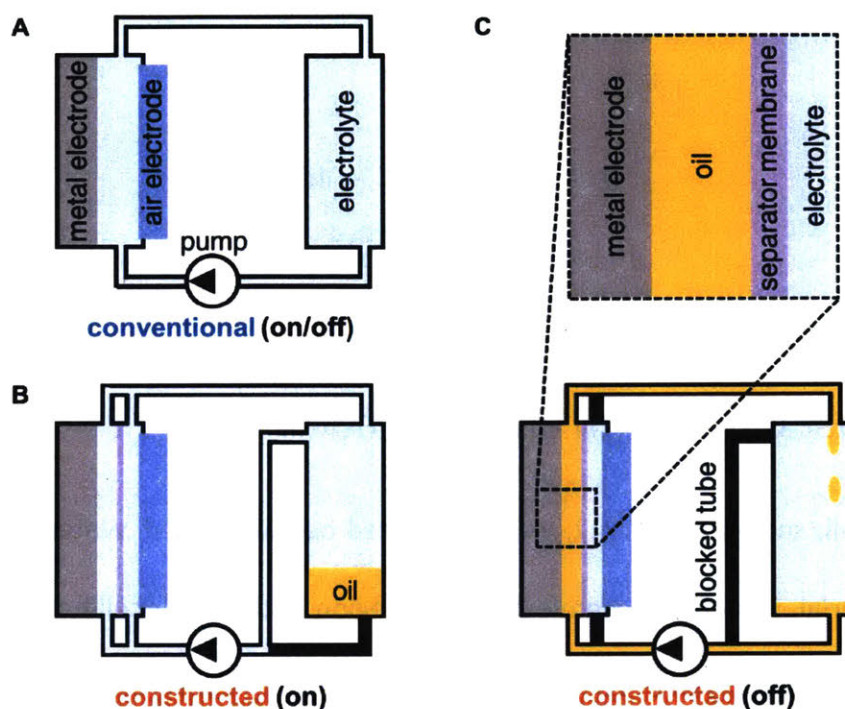
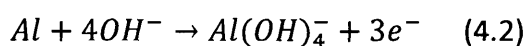
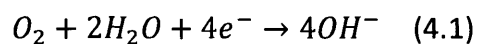


Fig. 4.1 Oil displacement method. (A) Schematic of conventional flowing electrolyte metal-air battery [61], [75], [88]. (B) Schematic of constructed oil displacement system for a flowing electrolyte metal-air battery. Electrolyte is continuously pumped during operation. When not in use, oil is pumped to displace the corrosive electrolyte for a specified duration. (C) Schematic of constructed oil displacement system when not in use with a magnified view of the interfaces of the metal electrode and separator membrane.

With this design, prolonged pauses in discharge along with high power and energy density could be enabled. The redesigned system achieves high power and energy density by using an aqueous electrolyte and enables ultra-low open-circuit corrosion rates because the oil dramatically

reduces the diffusion rate of corrosive electrolyte to the negative electrode surface. To prove this concept, a primary flowing-electrolyte Al-air battery was constructed (Fig. 4.2). The positive electrode is the air electrode consisting of carbon particles pressed on a metal mesh with a catalyst resulting in a reduction reaction (Eq. 4.1). The negative electrode is typically a plate of aluminum, which oxidizes during discharge (Eq. 4.2).



4.3 Al-Air Test Cell Design and Operation

The Al-air test cell, shown in Fig. 4.2, was 3D printed out of Somos® WaterShed XC 11122, a transparent material. The electrochemically active region of the Al-air cell had a width of 2 mm, a height of 7 mm, and a length of 20 mm. The Al-air cell with the separator membrane consisted of two channels, divided by the separator membrane, with widths of 2 mm, heights of 3.5 mm, and lengths of 20 mm. The active geometric surface area of the air electrode for both Al-air cells was 0.333 cm² and was the reference geometric area for current and power densities as the air electrode was the limiting electrode. Gaskets were laser cut out of silicone rubber sheets (McMaster-Carr). The negative electrode was 0.25-mm-thick 99.999% aluminum foil (Sigma-Aldrich). The electrolyte was 4 M sodium hydroxide (Sigma-Aldrich) with 0.05 M sodium stannate trihydrate (Sigma-Aldrich), a corrosion inhibitor [44]. The positive electrode was QSI-Nano® manganese gas diffusion air electrode (Quantum Sphere).

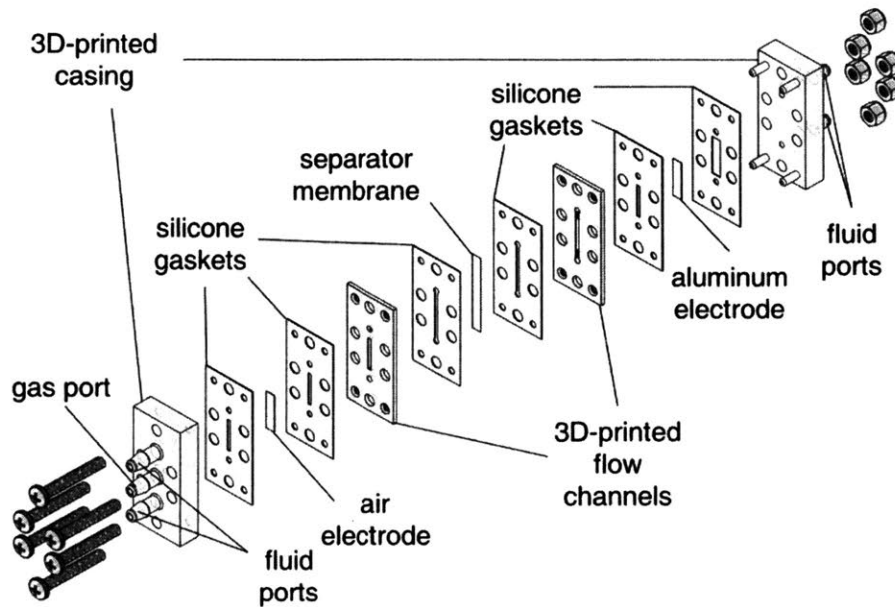


Fig. 4.2 Exploded view of Al-air test cell. During discharge, electrolyte is continuously pumped through the battery via the “fluid ports,” and atmospheric air is fed into the “gas port.”

During operation, electrolyte temperature was controlled to $60 \pm 5^\circ\text{C}$ using a water bath during discharge and was left to cool down to room temperature when inactive. Atmospheric air was fed into the air electrode and held at a pressure of $138 \text{ kPa} \pm 7 \text{ kPa}$. The tested separator membranes were Advantec MFS, Inc. polytetrafluoroethylene (PTFE) membrane, which was commercially modified to be hydrophilic, with $1.0\text{-}\mu\text{m}$ pore diameters and polypropylene laminated and coated Celgard® 5550 microporous membrane with $0.065\text{-}\mu\text{m}$ pore diameters. The tested displacing oils were 50-cSt silicone heat transfer fluid (Clearco) and general-purpose lubricant (GPL) 101 Krytox™, a perfluoropolyether (PFPE) oil.

For the conventional Al-air battery, no separator membrane was present, and the electrolyte flow rate was 654 ml min^{-1} . For the constructed design with a separator present, the flow rate was 488 ml min^{-1} . The oil-displacement flow rate that occurred in only one side of the separator membrane was 351 ml min^{-1} . Pumping speeds were selected to approximately match the pumping power of the constructed cell with the separator membrane operating at a flow rate of 488 ml min^{-1} . Oil pumping times were 50 s total and consisted of 30 s of forward pumping followed by 10 s in reverse and then 10 s forward. Occasionally after the initial pumping regime, remaining electrolyte would migrate to the top of the cell resulting in an open-circuit voltage near 1.8 V after approximately an hour. When this occurred, oil was pumped into the cell for an additional 30 s so that a floating voltage was thereafter maintained. For the conventional cell when no current was being drawn during the test shown in Fig. 4.6, the electrolyte flow rate was 17 ml min^{-1} corresponding to the lowest possible flow rate achievable on the used peristaltic pump to appropriately vent evolved hydrogen from the corrosion reaction.

4.4 Pumping and Air-Feed Power Requirements

The power required to pump electrolyte and feed air into the cathode was estimated to be less than 3% of the electrochemical power produced for a scaled-up Al-air battery pack with the hydrophilic PTFE separator membrane, which is comparable with values reported in the literature for large Al-air battery packs [61]. Al-air battery packs have used airlift pumps [61] that provide both electrolyte flow and air pressure to the positive electrode. For experimental ease, however, the electrolyte was pumped via a peristaltic pump, and pressurized atmospheric air was fed into the air electrode [88]. Larger current densities generally benefit from higher electrolyte flow

rates. While the flow rate could be optimally tuned to achieve minimal energy losses for different current densities, for simplicity, the selected electrolyte flow rate Q for all tests with the separator was 488 ml min^{-1} . The two channels, therefore, experienced flow rates of 244 ml min^{-1} .

$$Re_{D_H} = \frac{\rho v_{ave} D_H}{\mu} \quad (4.3)$$

The Reynolds number (Eq. 4.3) of each channel can be calculated with the following information. The density, ρ , and viscosity, μ , of 4 M sodium hydroxide at 60°C are 1132 kg m^{-3} and 1.09 mPa s respectively. The hydraulic diameter, D_H , for each channel was 0.0025 m . The average flow velocity, v_{ave} , equaled 0.581 m s^{-1} . These values yielded a Reynolds number with respect to hydraulic diameter of 1536, which generally implies laminar flow. It is assumed that pumping losses were dominated by the pressure drop in the interelectrode gaps of the battery. For a scaled-up Al-air battery pack [25], 2-mm-interelectrode gaps, square geometric electrode surfaces with side lengths of 20.7 cm, and 136 cells in the pack were assumed.

To estimate the losses due to pumping either during discharge or oil displacement, the Reynolds numbers of the prototype were matched to those for the scaled-up pack to calculate the associated pressure drop using the full-sized Al-air battery pack dimensions. Pressure losses were calculated using Eq 4.4.

$$\Delta P = f \frac{L}{D_H} \frac{\rho v_{ave}^2}{2} \quad (4.4)$$

The pressure drop, ΔP [Pa], is related to the friction factor, f [unitless], channel length, L [m], hydraulic diameter, D_H [m], fluid density, ρ [kg m⁻³], and average flow velocity, v_{ave} [m s⁻¹]. The friction factor is $n * Re_{D_H}^{-1}$, where n [unitless] is 96 for parallel plates. The power consumed during pumping is the pressure drop multiplied by flow rate. Using equations 4.3 and 4.4 and a pumping efficiency of 70%, a pack-level electrolyte pumping power of 120 W during discharge was calculated along with an oil pumping power of 120 W. The pressure drop in each channel for the electrolyte and oil were calculated to be 2.0 kPa and 2.8 kPa respectively. Assuming a maximum electrolyte/oil displacement pumping time of 10 min for startup/shutdown, 20 Wh would be required for pumping.

Air pressure could be tuned for optimal energy efficiency, but for simplicity, all experiments were performed at a pressure of 138 kPa \pm 7 kPa. Air-feed power was calculated using Eq. 4.5.

$$P = \frac{\Delta P * Q_{air}}{\eta} \quad (4.5)$$

Power, P [W], is a function of efficiency, η [unitless], gauge pressure applied to the air electrode, ΔP [Pa], and air flow rate, Q_{air} [m³ s⁻¹]. The minimum air flow rate is governed by the rate at which oxygen is consumed at the air electrode. The added air pressure counteracts air-electrode flooding due to pressure created by the flowing electrolyte. For a current density of 150 mA cm_{geo}⁻², the stoichiometric oxygen flow rate for the pack would be 24 l min⁻¹ with an applied gauge pressure, ΔP , of 138 kPa. Assuming double that flow rate to accommodate oxygen penetration through the membrane and a pumping efficiency, η , of 0.7, the estimated air feed power was

160 W. Under the stated assumptions, the estimated combined pumping and air feed losses would be 2.5% of the electrochemical power generated by the Al-air pack at $150 \text{ mA cm}_{\text{geo}}^{-2}$.

4.5 Oil and Separator Membrane Selection

To appropriately select a separator membrane and displacing oil, principles from underwater oleophobicity and thin film rupture theory were used. A two-phase Young equation (Eq. 4.6) can relate the wetting properties of fluids in air to the wetting properties of those fluids submerged in a different fluid [89].

$$\cos\theta_{o-e} = \frac{\gamma_{o-air}\cos\theta_{o-air} - \gamma_{e-air}\cos\theta_{e-air}}{\gamma_{o-e}} \quad (4.6)$$

The variable θ_{o-e} is the Young contact angle of an oil droplet surrounded by electrolyte on the negative electrode or separator membrane surface. The variables θ_{o-air} and θ_{e-air} are the Young contact angles of an oil and electrolyte droplet respectively surrounded by air on either the negative electrode or separator membrane surface. The surface tension of the oil and electrolyte are respectively γ_{o-air} and γ_{e-air} with an oil-electrolyte interfacial tension expressed as γ_{o-e} . Equation 4.6 suggests that to achieve underwater oleophobicity, where θ_{o-e} is greater than 90° , the right-hand term must be larger than the left-hand term necessitating the selection of an in-air hydrophilic negative electrode or separator membrane. Metal and metal oxides are commonly hydrophilic [90], and oils and hydrophilic separator membranes that are stable in electrolyte solutions can be identified. In addition, Eq. 4.6 suggests that low-surface tension

displacing oils are also more likely to display underwater oleophobicity than high surface tension oils.

Thin film rupture theory explains how oil can be effectively displaced from a surface that displays underwater oleophobicity. An oil with an advancing and receding underwater contact angle greater than 90° implies that the negative electrode or separator membrane are in lower energy states when they are wetted by the electrolyte than when they are wetted by the oil. This electrolyte preference facilitates the rupture of thin oil films on the negative electrode and separator surfaces [91]. Perturbations along with flow instabilities such as Saffman-Taylor [92], Kelvin-Helmholtz [93], Rayleigh-Taylor [94], [95], and van der Waals [91] displace the oil from the surfaces during electrolyte pumping. For oil displacement of electrolyte, the bulk electrolyte is displaced by the flowing oil that thins the remaining electrolyte films, which are eventually consumed by corrosion on the negative electrode with sufficient time. It should be noted that oil-surface combinations with receding contact angles less than 90° could also be fouling resistant. The less-than- 90° receding contact angle may be due to pining caused by surface roughness of the separator membrane or electrode. The theoretical Young contact angle determines the wetting preference of the oil-surface system and can be approximated from advancing and receding contact angles [96].

Selected separator membranes should also suppress the passage of the oil through the membrane at appropriate pumping pressures. The Young-Laplace equation (Eq. 4.7) can estimate

the pressure differential, ΔP , required for oil to leak through a circular pore with a diameter D in a separator membrane given an interfacial tension between the oil and electrolyte of γ_{o-e} .

$$\Delta P = \frac{4\gamma_{o-e}}{D} \quad (4.7)$$

The measured interfacial tension between the electrolyte and 50-cSt silicone oil and the electrolyte and PFPE oil both at 60°C was $34.8 \pm 0.1 \text{ mN m}^{-1}$ and $61.6 \pm 0.1 \text{ mN m}^{-1}$ respectively. The interfacial tension between the PFPE oil and electrolyte was measured using the pendant drop method with a Ramé-Hart goniometer in a temperature-controlled chamber held at 60.0°C. A 2-3 mm diameter droplet of PFPE oil was injected into an electrolyte bath. Ten photos were taken of the shape of the droplet in 1-s intervals to calculate the interfacial tension resulting in 10 interfacial-tension measurements using the Ramé-Hart software. For example, commercially available pore diameters for hydrophilic PTFE membranes range from 0.1 to 1 μm . If severe thermal expansion of 100% due to numerous heating cycles is assumed [97], 2- μm pore diameters would allow for pressures of 123 kPa, which is two orders of magnitude higher than necessary pumping pressures as shown in section 4.3 Al-Air Test Cell Design and Operation.

Motivated by these principles, low-surface tension silicone heat transfer fluid and PFPE oil were identified as potential displacing oils along with a hydrophilic membrane, Celgard® 5550, with 0.065- μm pores and an Advantec MFS, Inc. hydrophilic PTFE membrane with 1- μm pores as separator-membrane candidates. The selected oils have working temperatures between -40 and 104°C and cannot saponify in high-pH electrolytes because they contain no triglycerides. The

membranes were also selected for their chemical compatibility. The wetting properties of the oils on the membranes and electrode surfaces submerged in electrolyte were measured by the sessile drop technique to identify a fouling-resistant combination (Fig. 4.3).

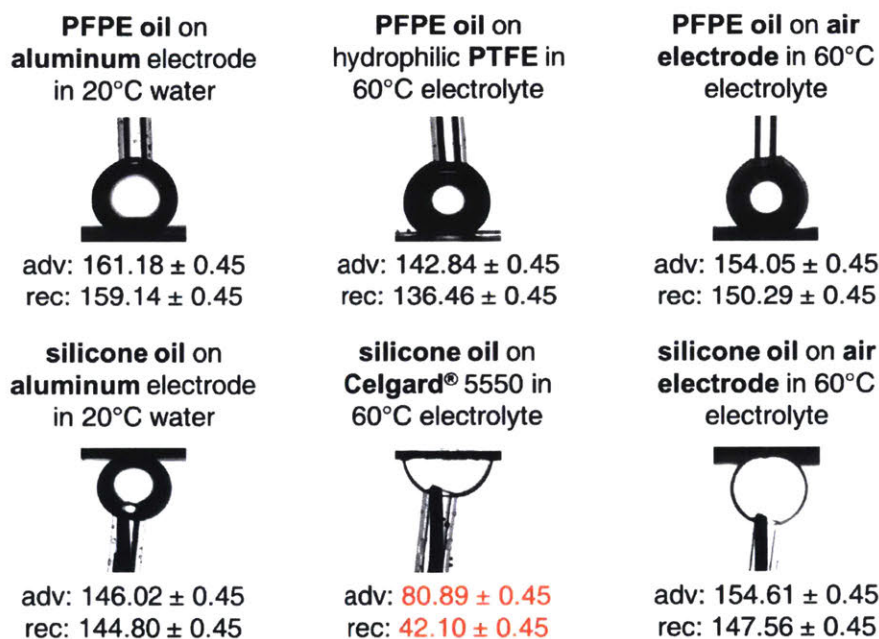


Fig. 4.3 Contact angle images with advancing and receding contact angle values. All systems displayed underwater oleophobicity except for the silicone-Celgard® combination.

Advancing and receding contact angles of PFPE and silicone oil observed in an electrolyte solution were measured using the add-and-remove-volume method on a Ramé-Hart goniometer. Photos were taken as the volume of the droplets were increased and decreased 5 times at rates of $0.25 \mu\text{l min}^{-1}$. Temperature was controlled to 60.0°C using a temperature controlled chamber. The aluminum electrode was covered in electrolyte for one minute to simulate the surface state of the electrode after some discharge, and then contact angles were measured on its surface. For

contact angles on the aluminum electrode, no sodium hydroxide and sodium stannate were used, and the temperature was kept at room temperature to stop hydrogen evolution during the contact angle experiments.

It should be noted that the air electrode displayed underwater oleophobicity but would be wetted by the oil if electrolyte significantly evaporated through the air electrode. To avoid the risk of air-electrode fouling via electrolyte evaporation, an underwater oleophobic separator membrane was used to allow for continuous air-electrode hydration. The pictures in Fig. 4.3 include the injecting needles because the droplets would not sufficiently adhere to the surfaces except in the case of the silicone oil on Celgard® 5550. The injection needles come from below for the silicone oil because the silicone oil is lighter than the electrolyte meaning the oil floats upward while the PFPE oil is heavier than the electrolyte and consequently sinks. The environmental fluid for the aluminum electrode was pure water at 20°C because elevated temperatures or the presence of either NaOH or Na₂SnO₃ would induce hydrogen evolution.

The contact angle analysis results implied that the PFPE-PTFE combination would resist fouling. Both the silicone and PFPE oil displayed underwater oleophobicity on the aluminum electrodes (Fig. 4.3). On the aluminum electrode, the silicone oil had advancing and receding contact angles of $146.02 \pm 0.45^\circ$ and $144.80 \pm 0.45^\circ$ respectively, and the PFPE oil achieved advancing and receding contact angles of $161.18 \pm 0.45^\circ$ and $159.14 \pm 0.45^\circ$. The silicone oil, however, wetted the Celgard® 5550 membrane (Fig. 4.3) with advancing and receding contact angles of $80.98 \pm 0.45^\circ$ and $42.10 \pm 0.45^\circ$, which suggested that the Celgard® 5550 membrane was not sufficiently

hydrophilic to display underwater oleophobicity. The silicone-Celgard® combination would therefore foul according to thin film rupture theory. In contrast, the PFPE oil displayed underwater oleophobicity on the hydrophilic PTFE membrane with advancing and receding contact angles of $142.84 \pm 0.45^\circ$ and $136.46 \pm 0.45^\circ$ implying fouling resistance.

On-off cycling with the silicone-Celgard® and PFPE-PTFE combinations was performed (Fig. 4.4) and yielded results suggesting that the silicone-Celgard® combination fouled while the PFPE-PTFE combination resisted fouling. Current densities of $150 \text{ mA cm}_{\text{geo}}^{-2}$ were drawn for 25 min with 1-h pauses where no current was drawn. At the start of each pause, the displacing oil was pumped into the battery for 50 s. Before the following discharge, electrolyte was pumped into the battery for 50 s. After the silicone oil was pumped in, subsequent discharge voltages were negative suggesting that the silicone oil fouled the Celgard® membrane (Fig. 4.4A). The total energy density achieved by the silicone-Celgard® combination was $0.66 \pm 0.08 \text{ Wh g}_{\text{Al}}^{-1}$. In contrast, the PFPE-PTFE combination showed positive voltages after each pause (Fig. 4.4B). The total energy density achieved by the PFPE-PTFE combination was $3.55 \pm 0.08 \text{ Wh g}_{\text{Al}}^{-1}$, which is comparable to the energy density achieved by discharging the battery without pauses and without introducing oil, $3.54 \pm 0.08 \text{ Wh g}_{\text{Al}}^{-1}$ (Fig. 4.5). These energy-density results implied that the hydrophilic PTFE membrane resisted fouling by the PFPE oil. The PTFE-PFPE combination was therefore selected to perform a 24-day on-off cycling endurance test (Fig. 4.6).

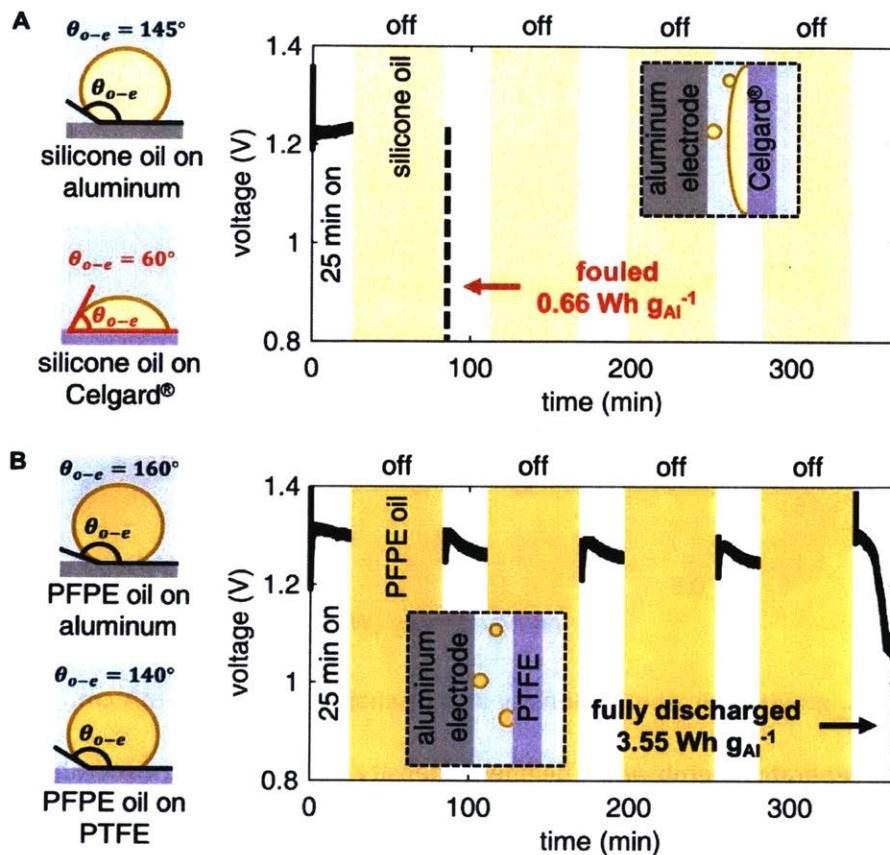


Fig. 4.4 Selecting a displacing oil and separator membrane. (A) Contact angle schematics of silicone oil on aluminum electrode (top left) and on Celgard® membrane (bottom left). Voltage vs. time for on-off cycling using silicone oil and Celgard® membrane (right). (B) Corresponding experiments presented in Fig. 4.4A using a PFPE oil and hydrophilic PTFE membrane. The corresponding insert depicts a fouling-resistance hydrophilic PTFE membrane and aluminum electrode.

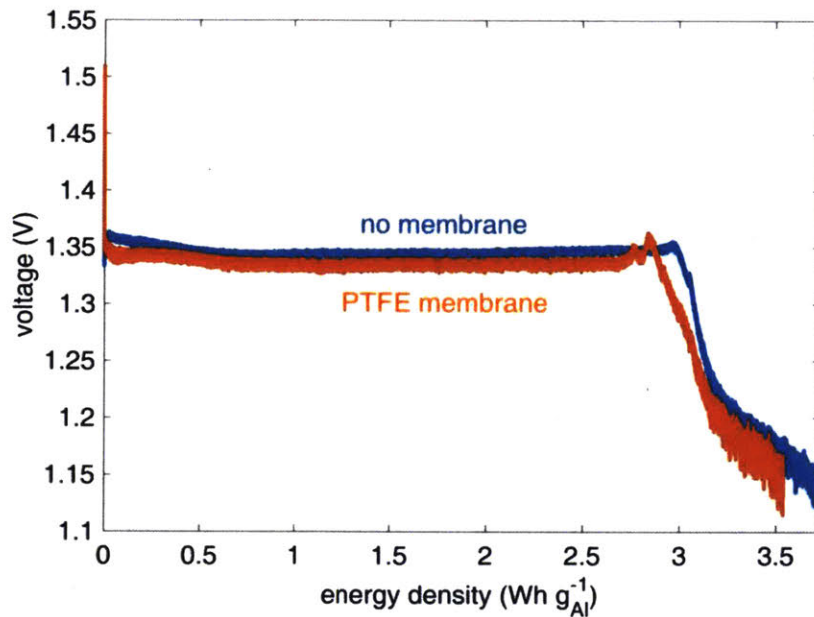


Fig. 4.5 Voltage vs. gravimetric energy density at a discharge rate of $150 \text{ mA cm}_{\text{geo}}^{-2}$ with and without hydrophilic PTFE separator membrane. The energy density achieved with the membrane was $3.54 \pm 0.08 \text{ Wh g}_{\text{Al}}^{-1}$ and without $3.75 \pm 0.08 \text{ Wh g}_{\text{Al}}^{-1}$.

4.6 Endurance Testing

The useable energy density of a flowing-electrolyte Al-air battery was increased by 420% with the use of an oil displacement system tested over the course of 24 days (Fig. 1D). Current densities of $150 \text{ mA cm}_{\text{geo}}^{-2}$ were drawn for 5-min intervals with 24 or 72-h pauses in between (16). During pauses for the conventional cell, the electrolyte remained in the interelectrode gap with corrosion current near $10 \text{ mA cm}_{\text{geo}}^{-2}$. For the constructed cell, a PFPE oil was pumped into the cell for 50 s at the start of each pause to displace the corrosive electrolyte. Once the oil displaced the electrolyte, corrosion currents dropped to an estimated value of $0.01 \text{ mA cm}_{\text{geo}}^{-2}$. Before each discharge, the electrolyte was pumped back into the cell for 50 s. At the start of day

3, the conventional cell yielded a negative voltage when $150 \text{ mA cm}_{\text{geo}}^{-2}$ was drawn. The exposed aluminum electrode was dissolved through its thickness at that time, which was monitored through the transparent battery casing. The resulting energy density of the conventional cell was $0.40 \pm 0.07 \text{ Wh g}_{\text{Al}}^{-1}$. In contrast, the constructed cell lasted more than 24 days and yielded an energy density of $2.08 \pm 0.07 \text{ Wh g}_{\text{Al}}^{-1}$, an improvement of 420%. The constructed cell achieved a higher energy density because of the 1,000-fold reduction (10 to 0.01 mA cm^{-2}) in open-circuit corrosion current caused by the oil. For a scaled-up 0.5-cm-thick planar aluminum electrode, the oil displacement method could result in a self-discharge rate less than 0.4% a month.

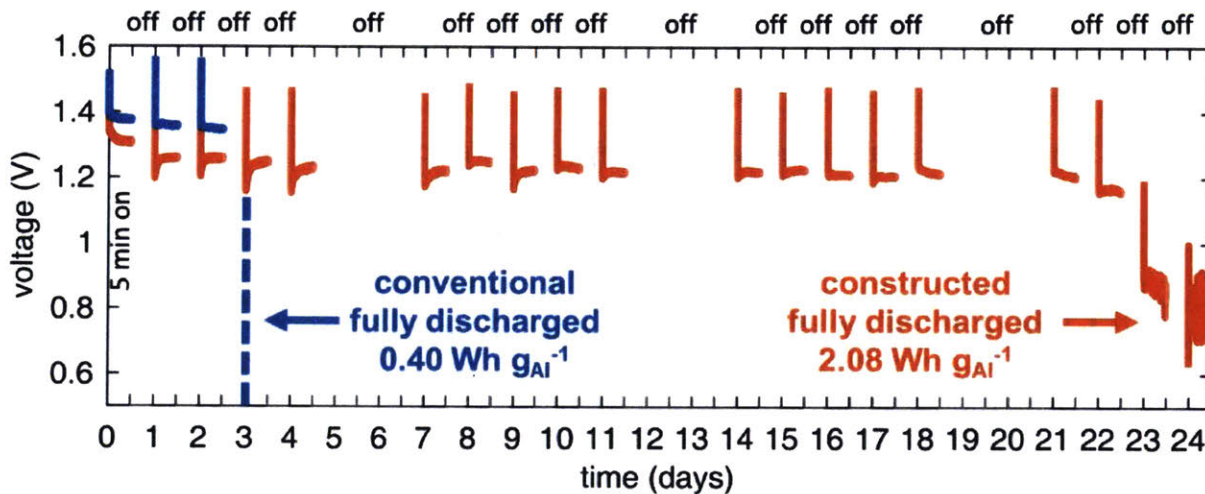


Fig. 4.6 24-day on-off cycling. Voltage vs. time for on-off cycling of a primary Al-air battery with the conventional cell design (Fig. 4.1A) and the constructed cell design (Fig. 4.1B, Fig. 4.1C).

The open-circuit corrosion rate of the aluminum in direct contact with the electrolyte was measured using the mass-loss method. At 20 °C, a 1-cm-by-1-cm piece of the aluminum foil was dropped into 80 ml of electrolyte and left to corrode for 20 min. The mass of the foil was measured three times before and after electrolyte submersion. With Faraday's law of electrolysis, an open-circuit corrosion rate of $13.4 \pm 2.1 \text{ mA cm}_{\text{geo}}^{-2}$ was calculated, which matches values in the literature using the same corrosion inhibitor [44]. Corresponding standard deviation values represent three independent mass measurements before and after electrolyte submersion. The open-circuit corrosion of aluminum surrounded in oil was calculated using Fick's first law of diffusion with a diffusivity constant of $10^{-9} \text{ m}^2 \text{ s}^{-1}$ [98] and a maximum concentration of $0.0014 \text{ mol l}^{-1}$ of water in PFPE oil at 20 °C [99]. Assuming a 1.0 mm distance between the negative electrode and underwater oleophobic separator membrane, a corresponding corrosion rate of $0.013 \text{ mA cm}_{\text{geo}}^{-2}$ is calculated with Faraday's law of electrolysis [22].

4.7 Cell Characterization

The performance of the constructed cell with the oil displacement system was characterized and found to be comparable to the performance of Al-air cells in the literature. The voltage (Fig. 4.7A, Fig. 4.8) and capacity (Fig. 4.7B, Fig. 4.9) was measured as a function of current density. The prototype with the hydrophilic PTFE membrane achieved a peak power density of $300 \pm 17 \text{ mW cm}_{\text{geo}}^{-2}$ (Fig. 4.7A, Fig. 4.10) and energy density of $3.73 \pm 0.08 \text{ Wh g}_{\text{Al}}^{-1}$ (Fig. 4.12). Reported peak powers of flowing-electrolyte Al-air batteries with 2 to 3-mm interelectrode gaps range from 350 to 620 $\text{mW cm}_{\text{geo}}^{-2}$ and obtain peak energy densities near $4.3 \text{ Wh g}_{\text{Al}}^{-1}$ [25], [61] while prototypes with gaps near 10 mm achieve peak powers as low as $75 \text{ mW cm}_{\text{geo}}^{-2}$ depending on cell design

and operation [28]. The constructed prototype values can be attributed to the 7-mm interelectrode gap and to the added separator membrane. Without the separator membrane, the prototype reached a peak power of $350 \pm 17 \text{ mW cm}_{\text{geo}}^{-2}$ (Fig. 4.10). The large gap allowed for appropriate separator-membrane sealing. Production-level sealing methods such as laser or ultrasonic welding would enable smaller interelectrode gap sizes.

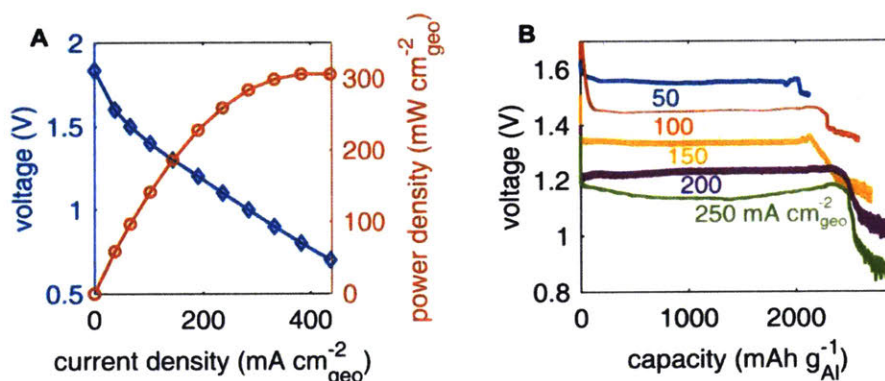


Fig. 4.7 Constructed-cell performance. (A) Voltage and power density vs. current density of the constructed primary aqueous Al-air battery using the hydrophilic PTFE membrane. (B) Voltage vs. capacity of the same battery used in Fig. 4.8A for discharging currents of 50, 100, 150, 200, and 250 $\text{mA cm}_{\text{geo}}^{-2}$.

The PFPE separator membrane, however, minimally impacted power and energy density for energy-efficient current densities below 250 $\text{mA cm}_{\text{geo}}^{-2}$ (Fig. 4.11). For example, at 150 $\text{mA cm}_{\text{geo}}^{-2}$ the power and energy density achieved with the separator membrane was $192 \pm 5 \text{ mW cm}_{\text{geo}}^{-2}$ and $3.54 \pm 0.08 \text{ Wh g}_{\text{Al}}^{-1}$. Excluding the separator membrane yielded an increase of only $7 \pm 6 \text{ mW cm}_{\text{geo}}^{-2}$ and $0.21 \pm 0.11 \text{ Wh g}_{\text{Al}}^{-1}$ (Fig. 4.10, Fig. 4.5).

Polarization curves were generated using a Biologic Potentiostat (Fig. 4.7A, Fig. 4.8). Current was measured while voltage was held constant at 0.1 V intervals. Current stabilized after 2 to 3 minutes for each voltage step. Measurements were taken 3 min after the electrolyte filled the interelectrode gap of the cell. Current densities were measured with respect to the geometric area of the exposed air electrode.

To measure capacity and energy density, the constructed prototype was discharged at 50, 100, 150, 200, and 250 mA cm_{geo}⁻² (Fig. 4.7B, Fig. 4.9). Discharge was stopped once exposed aluminum was no longer present, which could be detected by visual inspection with the transparent battery casing. The voltage would then drop to a lower voltage plateau that corresponded to the consumption of the aluminum pressed between the gaskets. Masses of the aluminum electrodes were measured three times before discharge and three times after discharge using a scale with an accuracy of 0.1 mg.

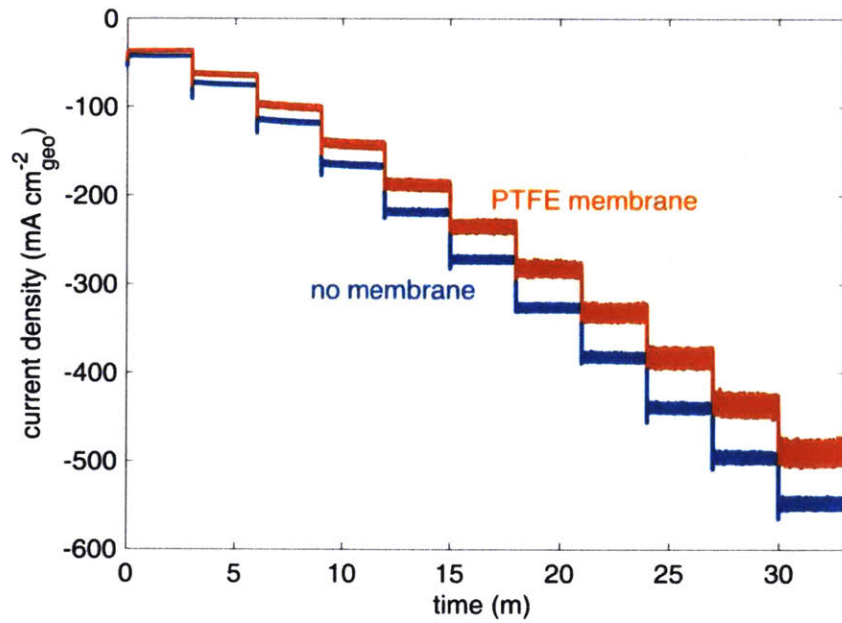


Fig. 4.8 Current density vs. time with and without hydrophilic PTFE separator membrane. Voltage was controlled from 0.6 to 1.6 V in 0.1 V intervals.

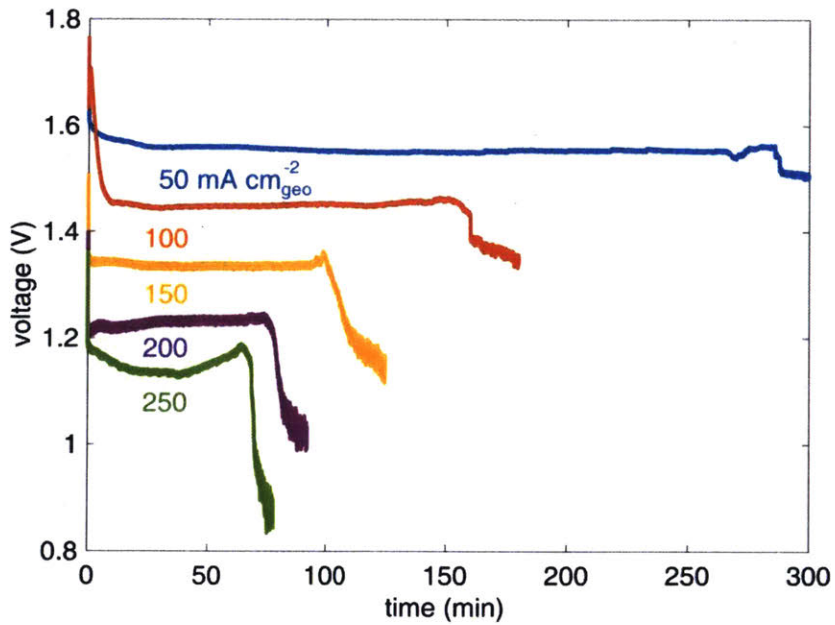


Fig. 4.9 Voltage vs. time with hydrophilic PTFE separator membrane. Current densities range from 50 to 250 mA cm_{geo}⁻².

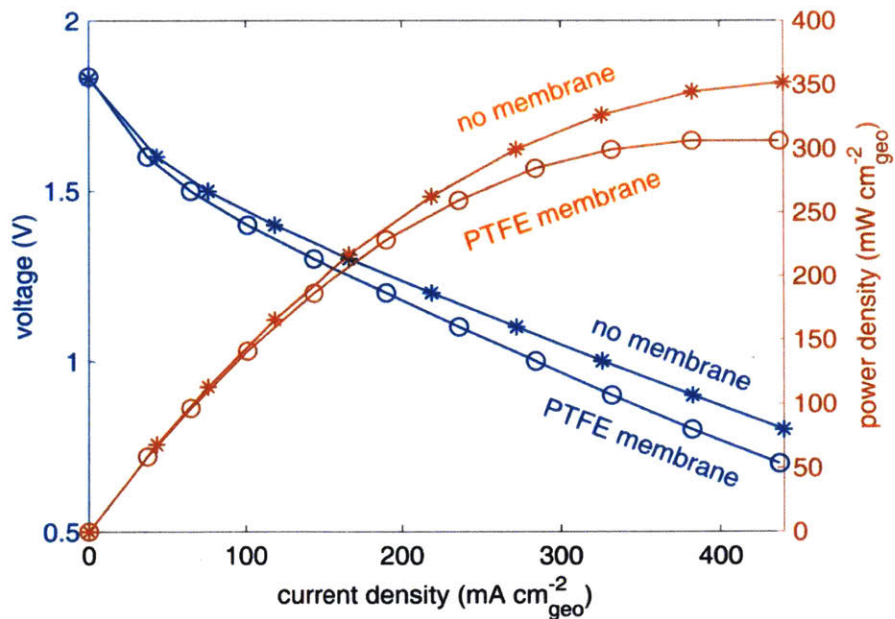


Fig. 4.10 Voltage and power density vs. current density with and without hydrophilic PTFE separator membrane.

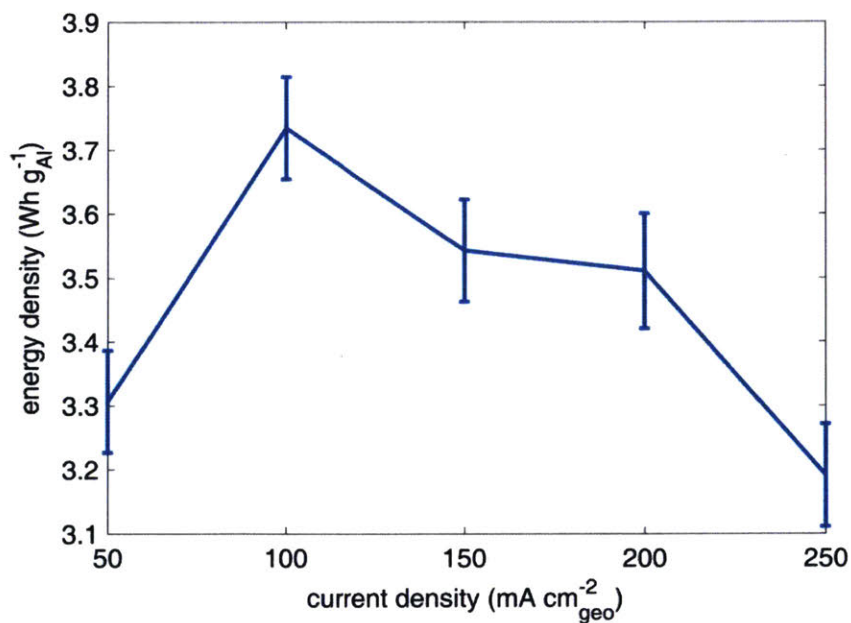


Fig. 4.11 Gravimetric energy density vs. current density with the hydrophilic PTFE separator membrane.

Error bars represent two standard deviations and are calculated from 6 independent measurements of anode mass (3 before and 3 after discharge) and one energy measurement per current density (Fig. 4.9).

4.8 Pack-Level Energy Density

The mass distribution of an Al-air battery pack with an oil displacement system was calculated using data from Al-air battery packs designed for electric vehicles (EVs) [25], [61]. Such packs achieved peak powers of 34.8 kW with system-level energy densities of 936 Wh l⁻¹ and 1300 Wh kg⁻¹ and total volumes and masses of 371 l and 267 kg [25]. These system-level energy densities, however, assumed that the battery was continuously discharged. To enable energy-efficient startup/shutdown capability, 20 l of displacing oil with 36 kg of mass assuming PFPE oil was used was added to the pack model. The added mass only represented 13% of the total mass of the pack (Fig. 4.12).

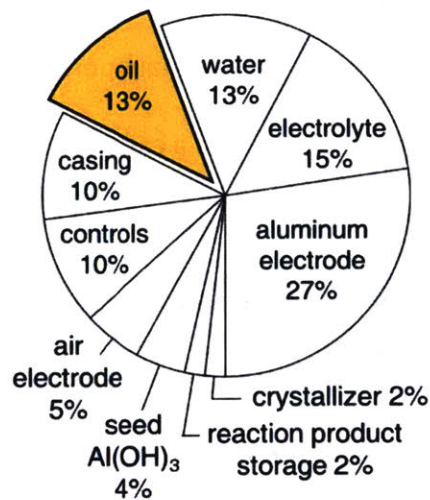


Fig. 4.12 Pack-level mass distribution. Estimated mass distribution of a primary Al-air battery pack [25] with the incorporated oil displacement system. The oil accounted for only 13% of the total mass of the system.

Scaled-up corrosion losses per shutdown cycle for an Al-air battery pack with an oil displacement system were calculated using data from the 24-day experiment (Fig. 4.6). The reduction in capacity with respect to the capacity achieved by continuous discharge (Fig. 4.5) was attributed to corrosion associated with the thin layer of electrolyte that remained on the aluminum electrode after bulk electrolyte displacement. Minimal change in energy density was observed when pauses were 1 h (Fig. 4.4) and minimal changes in voltage were observed between pauses that lasted 24-h and 72-h (Fig. 4.6). These observations suggested that little corrosion occurred after 1 h and that remaining electrolyte layers were fully consumed by corrosion after approximately 24 h. Equal volumes of remaining electrolyte on the negative electrode were therefore assumed after each discharge of the 24-day experiment and a loss of $14 \text{ g}_{\text{Al}} \text{ m}_{\text{geo}}^{-2}$ per pause was calculated. If $150 \text{ mA cm}_{\text{geo}}^{-2}$ is the normal operating current density, an approximate voltage of 1.22 V will be maintained (Fig. 4.6) with a capacity of $2.697 \text{ Ah g}_{\text{Al}}^{-1}$ (Fig. 4.7B). Assuming operation at the stated voltage and capacity, system-level corrosion yields a loss of 267 Wh per shutdown. In contrast, system-level pumping losses were estimated to be only 20 Wh per startup/shutdown cycle with the pumping regime used in the 24-day experiment. The order of magnitude difference in corrosion and pumping losses suggest that there is significant room for energy-density improvement by pumping optimization [100]. The corrosion and pumping losses per startup/shutdown cycle enable the calculation of useable system energy density as a function of the number of startup/shutdown cycles before complete discharge (Fig. 4.13).

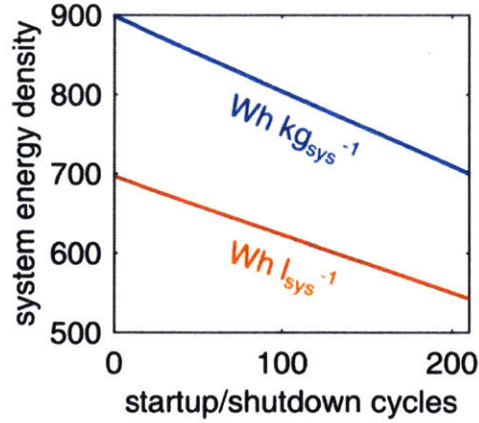


Fig. 4.13 Useable system energy density. Useable system energy density vs. number of startup/shutdown cycles that occur before complete discharge.

Useable pack-level energy densities ranging from 540-700 Wh l_{sys}⁻¹ and 700-900 Wh kg_{sys}⁻¹ (Fig. 4.13) were calculated with a standard operational power of 11 kW appropriate for a variety of applications. To calculate a lower-bound energy density limit, it was assumed that each startup/shutdown cycle yields corrosion-damage comparable to a 24-h shutdown. The useable system energy density, E_{sys} , is a function of the energy stored in the aluminum, E_{Al} , the number of startup/shutdown cycles, n , the losses due to corrosion and pumping per startup/shutdown cycle, c_{loss} and p_{loss} , and the system volume or mass that includes the oil displacement system, v_{sys} or m_{sys} , resulting in Eq. 4.8 for system volumetric energy density.

$$E_{sys} = \frac{E_{AL} - n(c_{loss} + p_{loss})}{v_{sys}} \quad (4.8)$$

Using the constructed prototype's power density, a current density of 150 mA cm_{geo}⁻² yields a pack power of 11 kW. Such powers are relevant for many technologies including off-grid power

units [74], industrial robots [101], and vehicular propulsion [102]. For example, an off-grid power unit that is fully discharged after only a few startup/shutdown cycles will have energy densities near $700 \text{ Wh l}_{\text{sys}}^{-1}$ and $900 \text{ Wh kg}_{\text{sys}}^{-1}$. In contrast, an electric vehicle (EV) or EV range extender that sustains approximately 200 startup/shutdown cycles before complete discharge would have energy densities near $540 \text{ Wh l}_{\text{sys}}^{-1}$ and $700 \text{ Wh kg}_{\text{sys}}^{-1}$ representing a significant increase in energy density with respect to a Li-ion battery pack (Li-ion pack: $225 \text{ Wh l}_{\text{sys}}^{-1}$, $120 \text{ Wh kg}_{\text{sys}}^{-1}$) [103].

The energy density of an EV Al-air battery pack with an oil displacement system is calculated using the following assumptions. The studied Al-air pack contained 83 kg of aluminum, which provides a range of 1600 km with 4 stops for water [25]. Using the average annual vehicle distance traveled per driver in the United States, the aluminum in the pack would be depleted in 35 days [104]. Assuming 6 startup/shutdown cycles a day [105], 210 startup/shutdown cycles would be required. To calculate a lower-bound energy density limit, it is assumed that each startup/shutdown cycle yielded corrosion damage comparable to a 24-h shutdown. If $150 \text{ mA cm}_{\text{geo}}^{-2}$ is the normal operating current density, an approximate voltage of 1.22 V will be maintained (Fig. 4.6) with a capacity of $2.697 \text{ Ah g}_{\text{Al}}^{-1}$ (Fig. 4.7B). Using the constructed prototype's power density, a current density of $150 \text{ mA cm}_{\text{geo}}^{-2}$ yields a pack power of 11 kW, which is sufficient for city driving [102]. The resulting energy density was 540 Wh l^{-1} and 700 Wh kg^{-1} accounting for pumping and corrosion losses due to 210 startup/shutdown cycles along with the added volume and mass of the displacing oil.

4.9 Pumping Optimization

Three forms of losses are considered during shutdown in this analysis: pumping losses, corrosion losses that occur during pumping, and corrosion losses that occur after pumping assuming there is still remaining electrolyte on the negative electrode surface. A parallel plate geometry is assumed with a channel length L , a channel height $2a$ ($2a \ll L$), or the variable a multiplied by a factor of 2, and a channel width b ($b \sim L$). Using Eq. 4.3 and 4.4 along with the definition of hydraulic diameter, $D_H = 4ab/(2a + b)$, pumping efficiency η , and a flow rate $Q = 2abv_{ave}$, the energy lost due to pumping oil to displace electrolyte is estimated as $E_p = Q\Delta Pt/\eta$ where t is pumping time. With substitutions performed, the result yields equation 4.9. It should be noted that the viscosity of the electrolyte and PFPE oil are similar values at 60 °C. For simplicity, the viscosity of the two fluids are assumed to be equal. If the oil has a higher viscosity than the electrolyte, viscous fingering should not occur when the oil displaces the electrolyte.

$$E_p = \frac{nQ^2L\mu(2a+b)^2t}{64\eta(ab)^3} \quad (4.9)$$

The losses due to corrosion that occur during pumping can be calculated using Faraday's law of electrolysis. The aluminum lost, however, must be converted to energy, which is achieved using the open-circuit corrosion rate I_c [$A\ m^{-2}$], the molar mass of aluminum, M_{Al} [$g\ mol_{Al}^{-1}$], the capacity of aluminum, C_{Al} [$Ah\ g_{Al}^{-1}$], an operational voltage V [V], and the Faraday constant F [$C\ mol^{-1}$]. With these variables, energy loss due to corrosion that occurs during pumping, E_{cdp} , is derived (4.10).

$$E_{cdp} = \frac{I_c b L M_{Al} C_{Al} V t}{3F} \quad (4.10)$$

The losses due to corrosion after pumping assuming electrolyte still clings to the negative electrode is derived using the equations describing laminar flow between parallel plates and Faraday's law of electrolysis. In Fig. 4.14, l represents the distance from the oil reservoir to the negative electrode. The variable L represents the length of the negative electrode.

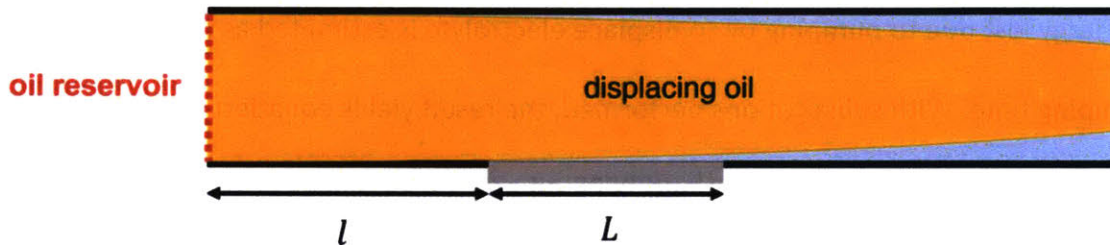


Fig. 4.14 Losses due to corrosion after pumping. Schematic of the interelectrode gap showing electrolyte that remains on the negative electrode.

The height of the electrolyte on the electrode surface can be approximated by assuming laminar flow between parallel plates and then solving for the height of the conventional parabolic velocity profile equation. As an upper-bound estimate, it will be assumed that the height of the electrolyte on the right corner of the electrode in Fig. 4.14 is the uniform height of electrolyte across the entire electrode surface. With this upper-bound approximation, the volume of electrolyte remaining on the negative electrode, V_{ele} , is shown in Eq. 4.11.

$$V_{ele} = abL \left(1 - \left(1 - \frac{128ab^3(l+L)}{nQ(2a+b)^2t} \right)^{\frac{1}{2}} \right) \quad (4.11)$$

With the volume of electrolyte left on the negative electrode, the amount of aluminum that will be corroded can be calculated with the conversion variables introduced in Eq. 4.10 along with the molar mass and density of water, M_w and d_w . The energy losses due to corrosion after pumping, E_{cap} , can be solved for (Eq. 4.12).

$$E_{cap} = \frac{d_w M_{Al} C_{Al} V}{3M_w} abL \left(1 - \left(1 - \frac{128ab^3(l+L)}{nQ(2a+b)^2t} \right)^{\frac{1}{2}} \right) \quad (4.12)$$

All three types of energy loss (4.9, 4.10, 4.12) can be summed and plotted as a function of pumping time for different flow rates (Fig. 4.15). As a case study, the following values were used to generate the plot in Fig. 4.15. The variable l is set to zero. The variables L and b are 0.21 m, and a is 0.0005 m. A low corrosion rate of 2.5 A m^{-2} is used. Total electrode thickness, which dictates the total energy stored in the battery referenced in percentage energy loss per shutdown, is 0.001 m. The flow rates are indicated in Fig. 4.15. When low flow rates and short pumping times are used, corrosion losses dominate. Alternatively, when high flow rates and long pumping times are used, pumping losses dominate. The presented equations represent a preliminary analysis that could be used to optimize flow rates and pumping times. Future studies, however, need to be performed to ensure that the presented analytical model matches empirical data.

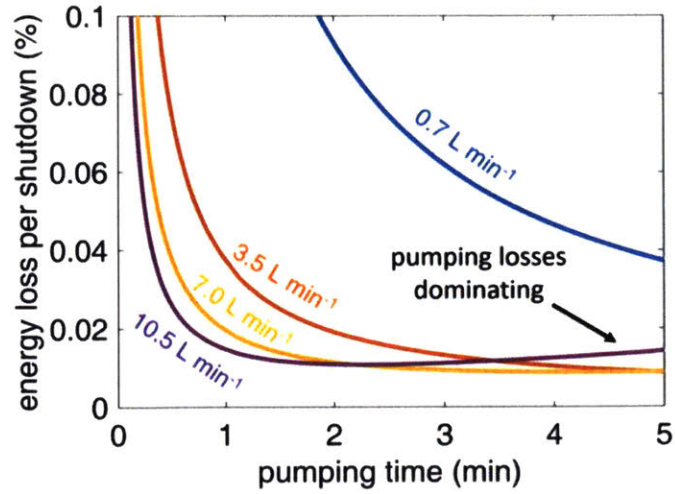


Fig. 4.15 Pumping and corrosion losses after shutdown. Percentage of energy lost per shutdown vs. pumping time. Corrosion losses dominate during low flow rates and short pumping times. Pumping losses dominate during high flow rates and long pumping times.

Chapter 5

Conclusion

5.1 Purpose, Importance, and Impact

The purpose of this thesis was to create an open-circuit corrosion mitigation method for metal-air batteries that enables high power and energy density and ultra-low open-circuit corrosion. The demonstrated oil-displacement method is important because it may further enable the practical implementation of metal-air batteries for applications that require significant power and energy density with prolonged pauses in discharge. The oil-displacement method could have significant impact because, in principle, it could be used in any of the metal-air batteries, aqueous or nonaqueous, or in other energy storage systems that suffer from corrosion if appropriate displacing oils and separator membranes are found using the discussed design principles. With the oil-displacement method, aqueous metal-air batteries that rely on abundant, broadly dispersed materials could provide safe, low-cost, sustainable primary (single use) and secondary (rechargeable) batteries for a variety of applications including grid-storage, backup power supplies, and vehicular propulsion.

5.2 Accomplishments

This thesis documents the design process used to invent the oil displacement method and presents multiple open-circuit corrosion mitigation concepts that could be appropriate for a variety of alternative applications. Specifically, the louver gasket and the concept involving electrolyte displacement via compressed air should dramatically reduce self-discharge but were not selected for further development due to desired system-level design specifications. Under different system-level design specifications, however, such design concepts could be useful.

The constructed primary Al-air battery prototype with the oil-displacement method achieved a high peak power and high energy density of $300 \pm 17 \text{ mW cm}_{\text{geo}}^{-2}$ and $3.73 \pm 0.08 \text{ Wh g}_{\text{Al}}^{-1}$ with an ultra-low open-circuit corrosion near $0.01 \text{ mA cm}_{\text{geo}}^{-2}$. Such an open-circuit corrosion rate yields a calculated self-discharge rate less than 0.4% per month assuming a 10 cm by 10 cm by 0.5 cm planar electrode that is continuously surrounded by electrolyte. This self-discharge rate is a 10-fold reduction in self-discharge in comparison to a Li-ion battery [4]. The oil displacement method consequently allowed for a 420% increase in useable energy density in an Al-air battery and was estimated to enable pack-level energy densities as high as 700 Wh l^{-1} and 900 Wh kg^{-1} . Such energy densities are significantly higher than those achieved by Li-ion battery packs ($225 \text{ Wh l}_{\text{sys}}^{-1}$, $120 \text{ Wh kg}_{\text{sys}}^{-1}$) [103].

The governing physics that explain the principles of oil displacement are presented. A two-phase Young equation and thin film rupture theory can be used to understand how the oil-displacement method operates. The selected displacing oil should display underwater oleophobicity on the

separator membrane and electrode surfaces. To achieve underwater oleophobicity, displacing oils will likely have low surface tensions, and electrodes and separator membranes should be hydrophilic. Separator membranes also need to have appropriately sized pores so that oil does not pass through them during pumping.

5.3 Future Work

This thesis tests the oil-displacement concept in a primary Al-air battery, but other metal-air batteries or other batteries that suffer from open-circuit corrosion could use the oil displacement method if appropriate displacing oils and separator membranes can be created or identified. Similar contact-angle analyses used in this study to select oils and membranes could be performed for iron, zinc, and magnesium electrodes. Outside of metal-air batteries, flow batteries may benefit from an adapted oil-displacement concept to mitigate shunt current [106].

While the selected silicone and PFPE oils and separator membranes appeared to display good chemical compatibility during testing, accelerated aging-tests could be performed to understand their long-term performance. The oils and separator membranes appear to be robust for approximately a month of use, but certain applications may require 5 or 10 years of chemical stability. In depth studies of how displacing oils and separator membranes degrade over time would be valuable. Accelerated aging could be achieved by high-temperature testing. Identifying when oils need to be reclaimed would also be necessary for system cost modeling.

This thesis presents a preliminary pumping optimization analysis, but such a model needs to be experimental verified. Beyond identifying ideal pumping speeds and times, pulse pumping regimes could significantly reduce corrosion losses due to shutdown [100]. Such techniques have been used in the food industry to effectively clean pipes. Similar methods may be adapted to enhance electrolyte displacement by oil. Additionally, the oil's underwater oleophobic contact angle can in part be controlled by the viscosity of the oil. Further optimization of displacing oil viscosity may also be useful to decrease corrosion losses during shutdown.

Identifying or creating low-cost oil and separator membranes are critical for practical implementation of the oil-displacement method. The hydrophilic PTFE membranes used in the study cost 130 \$ m⁻². PFPE oil can cost anywhere between 200-1000 \$ l⁻¹ depending on what type is used (reclaimed PFPE oil costs 235 \$ l⁻¹). Silicone oils, however, are significantly lower cost (25 \$ l⁻¹). Using the Al-air EV model as an approximation [25], the oil displacement system would cost approximately 30-100 \$ kWh⁻¹ with the PFPE-PTFE combination or 12 \$ kWh⁻¹ if a silicone-PTFE combination was achieved. Alternatively, if the hydrophilicity of the Celgard® membrane could be increased, the cost could be lowered even further as the PTFE membrane is relatively expensive. On a larger system level, cost and cradle-to-grave greenhouse-gas analyses should be performed on Fe-air, Zn-air, Al-air, and Mg-air using oil-displacement systems to identify appropriate applications. While some published works have started similar analyses [25], more work is needed in this area.

Works Cited

- [1] M. A. Rahman, X. Wang, and C. Wen, "High energy density metal-air batteries: A review," *J. Electrochem. Soc.*, vol. 160, no. 10, 2013.
- [2] D. U. Lee, P. Xu, Z. P. Cano, A. G. Kashkooli, M. G. Park, and Z. Chen, "Recent progress and perspectives on bi-functional oxygen electrocatalysts for advanced rechargeable metal-air batteries," *J. Mater. Chem. A*, vol. 4, no. 19, pp. 7107–7134, 2016.
- [3] Y. Li and J. Lu, "Metal-air batteries: Will they be the future electrochemical energy storage device of choice?," *ACS Energy Lett.*, vol. 2, no. 6, pp. 1370–1377, 2017.
- [4] L. Lu, X. Han, J. Li, J. Hua, and M. Ouyang, "A review on the key issues for lithium-ion battery management in electric vehicles," *J. Power Sources*, vol. 226, pp. 272–288, 2013.
- [5] B. Dunn, H. Kamath, and J.-M. Tarascon, "Electrical energy storage for the grid: A battery of choices," *Science*, vol. 334, no. 6058, pp. 928–35, Nov. 2011.
- [6] S. J. Gerssen-Gondelach and A. P. C. Faaij, "Performance of batteries for electric vehicles on short and longer term," *J. Power Sources*, vol. 212, pp. 111–129, 2012.
- [7] P. G. Bruce, S. A. Freunberger, L. J. Hardwick, and J.-M. Tarascon, "Li-O₂ and Li-S batteries with high energy storage," *Nat. Mater.*, vol. 11, no. 02, pp. 172–172, 2011.
- [8] B. Nykvist and M. Nilsson, "Rapidly falling costs of battery packs for electric vehicles,"

- Nat. Clim. Chang.*, vol. 5, no. April, pp. 100–103, 2015.
- [9] C. Davies, “Calls for lithium battery review after Boeing Dreamliner fire at Heathrow,” *The Guardian*, Aug-2015.
- [10] E.-Y. Jeong, “Samsung to recall Galaxy Note 7 smartphone over reports of fires,” *Wall Street Journal*, 02-Sep-2016.
- [11] B. News, “UN bans lithium batteries as cargo on passenger planes,” United Kingdom, 2016.
- [12] R. O’Brien and R. Nickel, “Battery-hungry world turns to South America’s ‘lithium triangle,’” *Reuters*, 15-Mar-2016.
- [13] J. Shankleman, T. Biesheuvel, J. Ryan, and D. Merrill, “We’re going to need more lithium,” *Bloomberg Businessweek*, Sep-2017.
- [14] A. Sonoc, J. Jeswiet, and K. V. Soo, “Opportunities to improve recycling of automotive lithium ion batteries,” in *Procedia CIRP*, 2015, vol. 29, pp. 752–757.
- [15] G. B. Haxel, J. B. Hedrick, and G. J. Orris, “Rare earth elements-critical resources for high technology,” 2002.
- [16] J. F. Cooper, “Continuous-feed electrochemical cell with nonpacking particulate electrode,” US Patent # 5,434,020, 1995.
- [17] G. Girishkumar, B. McCloskey, A. C. Luntz, S. Swanson, and W. Wilcke, “Lithium-air battery: Promise and challenges,” *J. Phys. Chem. Lett.*, vol. 1, no. 14, pp. 2193–2203, 2010.
- [18] D. R. Egan, C. Ponce de León, R. J. K. Wood, R. L. Jones, K. R. Stokes, and F. C. Walsh, “Developments in electrode materials and electrolytes for aluminum–air batteries,” *J.*

Power Sources, vol. 236, pp. 293–310, 2013.

- [19] Y. Ein-Eli, M. Auinat, and D. Starosvetsky, “Electrochemical and surface studies of zinc in alkaline solutions containing organic corrosion inhibitors,” *J. Power Sources*, vol. 114, no. 2, pp. 330–337, 2003.
- [20] Y. Lv, Y. Xu, and D. Cao, “The electrochemical behaviors of Mg, Mg-Li-Al-Ce and Mg-Li-Al-Ce-Y in sodium chloride solution,” *J. Power Sources*, vol. 196, no. 20, pp. 8809–8814, 2011.
- [21] D. Gelman, I. Lasman, D. Starosvetsky, and Y. Ein-Eli, “Aluminum corrosion mitigation in alkaline electrolytes containing hybrid inorganic/organic inhibitor system for power sources applications,” *J. Power Sources*, vol. 285, no. March 2016, pp. 100–108, 2015.
- [22] E. McCafferty, *Introduction to corrosion science*. Washington, DC: Springer, 2009.
- [23] P. Pei, K. Wang, and Z. Ma, “Technologies for extending zinc–air battery’s cyclelife: A review,” *Appl. Energy*, vol. 128, pp. 315–324, 2014.
- [24] M. Hilder, B. Winther-Jensen, and N. B. Clark, “The effect of binder and electrolyte on the performance of thin zinc-air battery,” *Electrochim. Acta*, vol. 69, pp. 308–314, 2012.
- [25] S. Yang and H. Knickle, “Design and analysis of aluminum/air battery system for electric vehicles,” *J. Power Sources*, vol. 112, pp. 162–173, 2002.
- [26] S. Zaromb, “The use and behavior of aluminum anodes in alkaline primary batteries,” *J. Electrochem. Soc.*, vol. 109, no. 12, p. 1125, 1962.
- [27] A. Sheik Mideen, M. Ganesan, M. Anbukulandainathan, K. B. Sarangapani, V. Balaramachandran, V. Kapali, and S. Venkatakrishna Iyer, “Development of new alloys of commercial aluminium (2S) with zinc, indium, tin, and bismuth as anodes for alkaline

- batteries," *J. Power Sources*, vol. 27, no. 3, pp. 235–244, 1989.
- [28] M. Rota, C. Comninellis, S. Moller, F. Holzer, and O. Haas, "Bipolar Al/O₂ battery with planar electrodes in alkaline and acidic electrolytes," *J. Appl. Electrochem.*, vol. 25, pp. 114–121, 1995.
- [29] M. J. Pryor, "Process for activating aluminum containing anode and anode," US Patent 3,228,866, 1966.
- [30] Y. Tang, L. Lu, H. W. Roesky, L. Wang, and B. Huang, "The effect of zinc on the aluminum anode of the aluminum-air battery," *J. Power Sources*, vol. 138, no. 1–2, pp. 313–318, 2004.
- [31] J. T. Reding and C. F. Schriber, "Indium-gallium-aluminum alloys and galvanic anodes made therefrom," 3,379,636, 1968.
- [32] D. D. Macdonald, S. Real, and M. Urquidi-Macdonald, "Evaluation of Alloy Anodes for Aluminum-Air Batteries: Corrosion Studies," *Electrochem. Sci. Technol.*, pp. 2397–2409, 1988.
- [33] P. W. Jeffrey, W. Halliop, and F. N. Smith, "Aluminum anode alloy," US Patent 4,751,086, 1988.
- [34] S. Zein El Abedin and A. O. Saleh, "Characterization of some aluminium alloys for application as anodes in alkaline batteries," *J. Appl. Electrochem.*, vol. 34, no. 3, pp. 331–335, 2004.
- [35] J. R. Moden and G. Perkons, "Aluminum anode alloy for primary high power density alkaline fuel cells and batteries," 4,150,204, 1979.
- [36] M. J. Pryor, D. S. Keir, and P. R. Sperry, "Aluminum alloy electrode," US Patent 3,240,688,

1966.

- [37] C. D. S. Tuck, "The electrochemical behavior of Al-Ga alloys in alkaline and neutral electrolytes," *J. Electrochem. Soc.*, vol. 134, no. December, p. 2970, 1987.
- [38] M. Nestoridi, D. Pletcher, J. A. Wharton, and R. J. K. Wood, "Further studies of the anodic dissolution in sodium chloride electrolyte of aluminium alloys containing tin and gallium," *J. Power Sources*, vol. 193, pp. 895–898, 2009.
- [39] K. K. Lee and K. B. Kim, "Electrochemical impedance characteristics of pure Al and Al-Sn alloys in NaOH solution," *Corros. Sci.*, vol. 43, no. 3, pp. 561–575, 2001.
- [40] M. J. Pryor, D. S. Keir, and P. R. Sperry, "Aluminum alloy for cathodic protection system and primary battery," 3,368,958, 1967.
- [41] G. P. Tarcy and R. M. Mazgaj, "Aluminum alloy and associated anode," US Patent 4,808,498, 1989.
- [42] G. P. Tarcy, "Aluminum alloy and associated anode and battery," US Patent 4,950,660, 1990.
- [43] M. Paramasivam, G. Suresh, B. Muthuramalingam, S. Venkatakrisna Iyer, and V. Kapali, "Different commercial grades of aluminum as galvanic anodes in alkaline zincate solutions," *J. Appl. Electrochem.*, vol. 21, pp. 452–456, 1991.
- [44] M. L. Doche, F. Novel-Cattin, R. Durand, and J. J. Rameau, "Characterization of different grades of aluminum anodes for aluminum/air batteries," *J. Power Sources*, vol. 65, pp. 197–205, 1997.
- [45] M. Paramasivam and S. Venkatakrisna Iyer, "Influence of alloying additives on corrosion and hydrogen permeation through commercial aluminum in alkaline solution," *J. Appl.*

- Electrochem.*, vol. 31, no. 1, pp. 115–119, 2001.
- [46] Y. J. Cho, I. J. Park, H. J. Lee, and J. G. Kim, "Aluminum anode for aluminum-air battery - Part I: Influence of aluminum purity," *J. Power Sources*, vol. 277, pp. 370–378, 2015.
- [47] L. Fan, H. Lu, J. Leng, Z. Sun, and C. Chen, "The study of industrial aluminum alloy as anodes for aluminum-air batteries in alkaline electrolytes," *J. Electrochem. Soc.*, vol. 163, no. 2, pp. A8–A12, 2016.
- [48] W. A. Ferrando, "Development of a novel composite aluminum anode," *J. Power Sources*, vol. 130, pp. 309–314, 2004.
- [49] R. Mori, "A new structured aluminium–air secondary battery with a ceramic aluminium ion conductor," *RSC Adv.*, vol. 3, no. 29, p. 11547, 2013.
- [50] R. Mori, "A novel aluminum–air secondary battery with long-term stability," *R. Soc. Chem.*, vol. 4, pp. 1982–1987, 2014.
- [51] X. Y. Wang, J. M. Wang, H. B. Shao, J. Q. Zhang, and C. N. Cao, "Influences of zinc oxide and an organic additive on the electrochemical behavior of pure aluminum in an alkaline solution," *J. Appl. Electrochem.*, vol. 35, no. 2, pp. 213–216, 2005.
- [52] D. D. Macdonald and C. English, "Development of anodes for aluminium/air batteries - solution phase inhibition of corrosion," *J. Appl. Electrochem.*, vol. 20, pp. 405–417, 1990.
- [53] S. I. Pyun, S. M. Moon, S. H. Ahn, and S. S. Kim, "Effects of Cl⁻, NO₃⁻ and SO₄²⁻ ions on anodic dissolution of pure aluminum in alkaline solution," *Corros. Sci.*, vol. 41, no. 4, pp. 653–667, 1999.
- [54] M. Katoh, "Aluminum-air battery," US Patent 3,563,803, 1971.
- [55] Y. Zhang, Y. Song, and Y. Wang, "Synergetic effect of stannate with o-aminophenol on

- inhibiting H₂ evolution of Al anode in strong alkaline media," *J. Shanghai Univ.*, vol. 11, no. 4, pp. 426–431, 2007.
- [56] N. A. F. Al-Rawashdeh and A. K. Maayta, "Cationic surfactant as corrosion inhibitor for aluminum in acidic and basic solutions," *Anti-Corrosion Methods Mater.*, vol. 52, no. 3, pp. 160–166, 2005.
- [57] A. M. Abdel-Gaber, E. Khamis, H. Abo-Eldahab, and S. Adeel, "Novel package for inhibition of aluminium corrosion in alkaline solutions," *Mater. Chem. Phys.*, vol. 124, no. 1, pp. 773–779, 2010.
- [58] M. A. Amin, S. S. A. El-Rehim, E. E. F. El-Sherbini, O. A. Hazzazi, and M. N. Abbas, "Polyacrylic acid as a corrosion inhibitor for aluminium in weakly alkaline solutions. Part I: Weight loss, polarization, impedance EFM and EDX studies," *Corros. Sci.*, vol. 51, no. 3, pp. 658–667, 2009.
- [59] J. Foucry, "Aluminum cell," US Patent 3,415,688, 1968.
- [60] P. S. D. Brito and C. A. C. Sequeira, "Organic inhibitors of the anode self-corrosion in aluminum-air batteries," *J. Fuel Cell Sci. Technol.*, vol. 11, no. 1, p. 011008, 2013.
- [61] E. Behrin, R. L. Wood, J. D. Salisbury, D. J. Whisler, and C. L. Hudson, "Design analysis of an aluminum-air battery for vehicle operations, transportation systems research," Livermore, CA, 1983.
- [62] Z. Zhang, C. Zuo, Z. Liu, Y. Yu, Y. Zuo, and Y. Song, "All-solid-state Al-air batteries with polymer alkaline gel electrolyte," *J. Power Sources*, vol. 251, pp. 470–475, 2014.
- [63] R. Revel, T. Audichon, and S. Gonzalez, "Non-aqueous aluminium-air battery based on ionic liquid electrolyte," *J. Power Sources*, vol. 272, pp. 415–421, 2014.

- [64] T. B. Reddy and D. Linden, *Linden's handbook of batteries*, 4th Editio. McGraw-Hill, 2011.
- [65] B. A. Abd-el-nabey, N. Khalil, and E. Khamis, "Alkaline corrosion of aluminum in water-organic solvent mixtures," *Surf. Technol.*, vol. 22, pp. 367–376, 1984.
- [66] A. Mukherjee and I. N. Basumallick, "Complex behavior of aluminum dissolution in alkaline aqueous 2-propanol solution," *J. Power Sources*, vol. 58, pp. 183–187, 1996.
- [67] H. B. Shao, J. M. Wang, X. Y. Wang, J. Q. Zhang, and C. N. Cao, "Anodic dissolution of aluminum in KOH ethanol solutions," *Electrochemistry*, vol. 10, no. 4, pp. 430–434, 2004.
- [68] J.-B. Wang, J.-M. Wang, H.-B. Shao, J.-Q. Zhang, and C.-N. Cao, "The corrosion and electrochemical behaviour of pure aluminium in alkaline methanol solutions," *J. Appl. Electrochem.*, pp. 753–758, 2007.
- [69] S. Muller, F. Holzer, J. Desilvestro, and O. Haas, "Aluminium alloys in sulfuric acid Part II: Aluminium-oxygen cells," *J. Appl. Electrochem.*, vol. 26, 1996.
- [70] S. Licht, G. Levitin, and C. Yarnitzky, "The effect of water on the anodic dissolution of aluminum in non-aqueous electrolytes," *Electrochem. commun.*, vol. 2, pp. 329–333, 2000.
- [71] G. M. Wu, S. J. Lin, and C. C. Yang, "Alkaline Zn-air and Al-air cells based on novel solid PVA/PAA polymer electrolyte membranes," *J. Memb. Sci.*, vol. 280, pp. 802–808, 2006.
- [72] A. A. Mohamad, "Electrochemical properties of aluminum anodes in gel electrolyte-based aluminum-air batteries," *Corros. Sci.*, vol. 50, no. 12, pp. 3475–3479, 2008.
- [73] J. M. Wang, J. B. Wang, H. B. Shao, X. X. Zeng, J. Q. Zhang, and C. N. Cao, "Corrosion and electrochemical behaviors of pure aluminum in novel KOH-ionic liquid-water solutions," *Mater. Corros.*, vol. 60, no. 12, pp. 977–981, 2009.

- [74] T. A. Dougherty, A. P. Karpinski, S. P. Lapp, R. N. J. Kallok, S. V. Natale, and A. G. Cannone, "Aluminum-air reserve power unit for use in a 6 kW standby power system," in *Telecommunications Energy Conference, 1995. INTELEC '95., 17th International, 1995*, pp. 821–827.
- [75] D. Tzidon and I. Yakupov, "Shutdown system for metal-air batteries and methods of use thereof," Patent US20150171494 A1, 2015.
- [76] B. M. L. Rao, R. Cook, W. Kobasz, and G. D. Deuchars, "Aluminum-air batteries for military applications," in *IEEE 35th International Power Sources Symposium, 1992*, no. 1, pp. 34–37.
- [77] L. Fan, H. Lu, and J. Leng, "Performance of fine structured aluminum anodes in neutral and alkaline electrolytes for Al-air batteries," *Electrochim. Acta*, vol. 165, pp. 22–28, 2015.
- [78] L. Fan and H. Lu, "The effect of grain size on aluminum anodes for Al-air batteries in alkaline electrolytes," *J. Power Sources*, vol. 284, pp. 409–415, 2015.
- [79] X. Yin, K. Yu, T. Zhang, H. Fang, H. Dai, H. Q. Xiong, and Y. L. Dai, "Influence of rolling processing on discharge performance of Al-0.5Mg-0.1Sn-0.05Ga-0.05In alloy as anode for al-air battery," *Int. J. Electrochem. Sci.*, vol. 12, no. 5, pp. 4150–4163, 2017.
- [80] L. Wang, W. Wang, G. Yang, D. Liu, J. Xuan, H. Wang, M. K. H. Leung, and F. Liu, "A hybrid aluminum/hydrogen/air cell system," *Int. J. Hydrogen Energy*, vol. 38, no. 34, pp. 14801–14809, 2013.
- [81] L. Wang, F. Liu, W. Wang, G. Yang, D. Zheng, Z. Wu, and M. K. H. Leung, "A high-capacity dual-electrolyte aluminum/air electrochemical cell," *RSC Adv.*, vol. 4, no. 58, pp. 30857–

- 30863, 2014.
- [82] M. Elimelech and W. a Phillip, "The future of seawater desalination: Energy, technology, and the environment.," *Science*, vol. 333, no. 6043, pp. 712–717, 2011.
- [83] T. Eggeman, "Sodium hydroxide," *Kirk-Othmer Encyclopedia of Chemical Technology*. John Wiley & Sons, Inc., pp. 1–16, 2011.
- [84] S. H. Yang and H. Knickle, "Modeling the performance of an aluminum-air cell," *J. Power Sources*, vol. 124, no. June, pp. 572–585, 2003.
- [85] T. Hiraki, M. Takeuchi, M. Hisa, and T. Akiyama, "Hydrogen production from waste aluminum at different temperatures, with LCA," *Mater. Trans.*, vol. 46, no. 5, pp. 1052–1057, 2005.
- [86] J. R. Davis, "27.8 Resistance of anodized aluminum," in *ASM Specialty Handbook - Aluminum and Aluminum Alloys*, ASM International, 1993.
- [87] B. J. Hopkins and D. P. Hart, "Corrosion mitigation in metal-air batteries," Patent WO2017176390A1, 2017.
- [88] M. Bockelmann, U. Kunz, and T. Turek, "Electrically rechargeable zinc-oxygen flow battery with high power density," *Electrochem. commun.*, vol. 69, pp. 24–27, 2016.
- [89] M. Liu, S. Wang, Z. Wei, Y. Song, and L. Jiang, "Bioinspired design of a superoleophobic and low adhesive water/solid interface," *Adv. Mater.*, vol. 21, pp. 665–669, 2009.
- [90] J. D. Bernardin, I. Mudawar, C. B. Walsh, and E. I. Franses, "Contact angle temperature dependence for water droplets on practical aluminum surfaces," *Int. J. Heat Mass Transf.*, vol. 40, no. 5, pp. 1–17, 2003.
- [91] A. Sharma, "Relationship of thin film stability and morphology to macroscopic

- parameters of wetting in the apolar and polar systems," *Langmuir*, vol. 9, no. 3, pp. 861–869, 1993.
- [92] K. V. McCloud and J. V. Maher, "Experimental perturbations to saffman-taylor flow," *Phys. Rep.*, vol. 260, no. 3, pp. 139–185, 1995.
- [93] P. G. Drazin and W. H. Reid, *Hydrodynamic stability*, 2nd ed. Cambridge University Press, 2004.
- [94] J. Fernandez, P. Kurowski, P. Petitjeans, and E. Meiburg, "Density-driven unstable flows of miscible fluids in a Hele-Shaw cell," *J. Fluid Mech.*, vol. 451, pp. 239–260, 2002.
- [95] X. Chen, B. J. Hopkins, A. Helal, F. Y. Fan, K. C. Smith, Z. Li, A. H. Slocum, G. H. McKinley, W. C. Carter, and Y.-M. Chiang, "A low-dissipation, pumpless, gravity-induced flow battery," *Energy Environ. Sci.*, vol. 9, no. 5, pp. 1760–1770, 2016.
- [96] R. Tadmor, "Line energy and the relation between advancing, receding, and Young contact angles," *Langmuir*, vol. 20, no. 18, pp. 7659–7664, 2004.
- [97] R. K. Kirby, "Thermal expansion of polytetrafluoroethylene (Teflon) from -190°C to $+300^{\circ}\text{C}$," *J. Res. Natl. Bur. Stand. (1934)*, vol. 57, no. 2, pp. 91–94, 1956.
- [98] M. H. Hilder and M. van den Tempe, "Diffusivity of water in groundnut oil and paraffin oil," *J. Chem. Technol. Biotechnol.*, vol. 21, pp. 176–178, 1971.
- [99] A. Chittofrati, D. Lenti, A. Sanguineti, M. Visca, C. M. C. Gambi, D. Senatra, and Z. Zhou, "Perfluoropolyether microemulsions," *Trends Colloid Interface Sci. III*, pp. 218–225, 1989.
- [100] K. Bode, R. J. Hooper, W. R. Paterson, D. I. Wilson, W. Augustin, and S. Scholl, "Pulsed flow cleaning of whey protein fouling layers," *Heat Transf. Eng.*, vol. 28, no. 3, pp. 202–209, 2007.

- [101] E. Abele, M. Weigold, and S. Rothenbücher, "Modeling and identification of an industrial robot for machining applications," *CIRP Ann. - Manuf. Technol.*, vol. 56, no. 1, pp. 387–390, 2007.
- [102] M. Gebrehiwot and A. Van den Bossche, "Starting requirements of a range extender for electric vehicles: based on a small size 4-stroke engine," *Int. J. Automot. Technol.*, vol. 16, no. 4, pp. 707–713, 2015.
- [103] K. G. Gallagher, S. Goebel, T. Greszler, M. Mathias, W. Oelerich, and V. Srinivasan, "Quantifying the promise of lithium-air batteries for electric vehicles," *Energy Environ. Sci.*, vol. 7, pp. 1555–1563, 2014.
- [104] A. Santos, N. McGuckin, H. Y. Nakamoto, D. Gray, and S. Liss, "2009 National household travel survey," Washington, DC, 2011.
- [105] P. T. Yu, W. Gu, R. Makharia, F. T. Wagner, and H. A. Gasteiger, "The impact of carbon stability on PEM fuel cell startup and shutdown voltage degradation," in *ECS Transactions*, 2006, vol. 3, no. 1, pp. 797–809.
- [106] B. J. Hopkins, "Mechanical design of flow batteries," Massachusetts Institute of Technology, 2013.